KfK 2968
Juni 1980

Numerical simulation of turbulent liquid metal flows in plane channels and annuli

G. Grötzbach
Institut für Reaktorentwicklung
Projekt Schneller Brüter

Kernforschungszentrum Karlsruhe

KERNFORSCHUNGSZENTRUM KARLSRUHE
Institut für Reaktorentwicklung
Projekt Schneller Brüter

KfK 2968

Numerical simulation of turbulent liquid metal flows in plane channels and annuli

Günther Grötzbach

Kernforschungszentrum Karlsruhe GmbH., Karlsruhe

Kernforschungszentrum Karlsruhe GmbH
ISSN 0303-4003

Abstract

The method of direct numerical simulation is used to study heat transfer and statistical data for fully developed turbulent liquid metal flows in plane channels and annuli. Subgrid scale models using one transport equation account for the high wave-number turbulence not resolved by the finite difference grid. A special subgrid-scale heat flux model is deduced together with an approximative theory to calculate all model coefficients. This model can be applied on the total Peclet number range of technical liquid metal flows. Especially it can be used for very small Peclet numbers, where the results are independent on model parameters.

A verification of the numerical results for liquid sodium and mercury flows is undertaken by the Nusselt number in plane channels and radial temperature and eddy conductivity profiles for annuli. The numerically determined Nusselt numbers for annuli indicate that many empirical correlations overestimate the influence of the ratio of radii. The numerical results for the eddy conductivity profiles may be used to remove these problems. The statistical properties of the simulated temperature fluctuations are within the wide scatter-band of experimental data. The numerical results give reasonable heat flux correlation coefficients which depend only weakly on the problem marking parameters.

Numerische Simulation turbulenter Flüssigmetallströmungen in Plattenkanälen und Ringspalten

Zusammenfassung

Die Methode der direkten numerischen Simulation wird zur Untersuchung des Wärmetransportes und statistischer Daten voll entwickelter Flüssigmetallströmungen in Plattenkanälen und Ringspalten benutzt. Mit Feinstrukturmodellen, für die eine zusätzliche Transportgleichung gelöst wird, werden die hochfrequenten Turbulenzanteile berücksichtigt, die nicht von den Maschennetzen aufgelöst werden können. Die Koeffizienten des vereinfachten Temperaturfeinstrukturmodells werden mittels einer Näherungstheorie berechnet. Das Modell kann auf den gesamten Peclet-Zahlen-Bereich technischer Flüssigmetallströmungen angewandt werden. Besonders vorteilhaft ist die Anwendung bei kleinen Peclet-Zahlen, weil dort die berechneten Temperaturfelder unabhängig von Modellparametern sind.

Die numerischen Ergebnisse für die Fluide Natrium und Quecksilber werden anhand der Nusselt-Zahlen für einen Plattenkanal, und anhand der radialen Profile der Temperatur und der turbulenten Wärmeaustauschgröße für Ringspalte verifiziert. Weiterhin zeigen die numerisch bestimmten Nusselt-Zahlen für Ringspalte, daß die meisten existierenden empirischen Beziehungen den Einfluß des Radienverhältnisses überschätzen. Die numerischen Ergebnisse für die Profile der turbulenten Wärmeaustauschgröße in diesen Kanälen können zur Beseitigung dieses Problems benutzt werden. Die statistischen Eigenschaften der simulierten Temperaturfluktuationen befinden sich innerhalb der weiten Streubänder experimenteller Daten. Die numerischen Ergebnisse liefern, im Gegensatz zu den meisten existierenden experimentellen Daten für Flüssigmetallströmungen, realistische Wärmestromkorrelationskoeffizienten, die zudem nur schwach von den Problemparametern abhängen.

List of Contents

List of figures

List of tables

Nomenclature

a	constant thermal diffusivity
c_p	constant specific heat capacity
C_T	subgrid scale heat flux coefficients
D	channel width, $R_2 - R_1$
E	turbulence energy, power spectral density
^jF	grid surface, $V/\Delta x_j$
Nu	Nusselt number
p	pressure
Pe	Peclet number, Re Pr
Pe^*	friction Peclet number, $Re^* Pr$
Pr	Prandtl number, ν/a
Pr_t	turbulent Prandtl number, $\varepsilon_m / \varepsilon_H$
$\dot{q}$	radial heat flux
$\dot{Q}$	specific volumetric heat source
$R_{1,2}$	inner, outer wall positions (Fig. 1)
Re	Reynolds number, $^V\langle u_1 \rangle 2D/\nu$
Re^*	friction Reynolds number, $u^* D/\nu$
t	time
T	temperature
T^+	universal temperature, T/T^*
T^*	heat flux temperature, $\dot{q}_w/(\rho\ c_p\ u^*)$
tsd	typical relative standard deviation

u_i	velocity component, indices refer to Fig. 1
u^*	friction velocity, $\sqrt{\tau_w/\rho}$
V	grid volume, $\Delta x_1 \; \Delta x_2 \; \Delta x_3$
χ , ϕ	periodicity lengths, see Fig. 1
Δx_i	grid widths
y	wall distance, mostly $y = R - R_1$

Greek symbols

δ_j	central finite difference operator
ε	turbulence dissipation
ε_H	eddy diffusivity for heat, $-\langle u_3'T'\rangle/\langle\partial T/\partial x_3\rangle$
ε_m	eddy diffusivity for momentum, $-\langle u_3'u_1'\rangle/\langle\partial u_1/\partial x_3\rangle$
ν	kinematic viscosity
ρ	constant specific density
γ_T	correction factor in the subgrid scale heat flux model, $\gamma_T \geq 1$
τ	radial shear stress

Indices

i,j	space indices, Fig. 1
t	turbulent
T	temperature
w	wall

operator for any quantity Y

$\langle Y \rangle$	time mean value
${}^{v}\langle Y \rangle$	channel volume mean value
${}^{v}\overline{Y}$	mesh cell volume mean value, $\int_{v} Y \, dv$
${}^{j}\overline{Y}$	mesh cell surface mean value, $\int_{^{j}F} Y \, d^{j}f$
$\overline{Y}$	average over both walls, cart. k=0, cyl. k=1, $(Y_{w1} R_1^k + Y_{w2} R_2^k) / (R_1^k + R_2^k)$
$\overline{Y}^{j}$	average value over two neighbouring grid values, $\overline{Y}^{j}(x_j) = (Y(x_{j+}) + Y(x_{j-}))/2$ j=1,2 $\overline{Y}^{j}(x_j) = (Y(x_{j+}) \Delta x_j(x_{j+}) R^k(x_{j+}) + Y(x_{j-}) \Delta x_j(x_{j-}) R^k(x_{j-}))$ $/(\Delta x_j(x_{j+}) R^k(x_{j+}) + \Delta x_j(x_{j-}) R^k(x_{j-}))$ j=3 with $x_{j+} = x_j + \Delta x_j/2$ and $x_{j-} = x_j - \Delta x_j/2$
Y'	fluctuating part of $Y' = Y - \langle Y \rangle$, and $Y' = Y - {}^{j}\overline{Y}$

1. Introduction

Working conditions in heat generating fuel elements of liquid metal fast breeder reactors extend from high Reynolds number turbulent flow for normal operation down to laminar flow in case of decay heat removal. Thus the models used to calculate the detailed temperature fields within the fuel elements have to account for the molecular and turbulent heat transport. Usually statistical turbulence models are applied which are based on the Reynolds equations. In most cases the unknown turbulent heat fluxes are modeled by the eddy diffusivity concept. The experimental determination of the eddy diffusivity for heat (= eddy conductivity) ε_H is a hard job due to many problems in using liquid metals. The theoretical way of applying formulations for the turbulent Prandtl number $Pr_t = \varepsilon_m/\varepsilon_H$, ε_m = eddy diffusivity for momentum, suffers from the same problem because the models have to be fitted by using experimental data.

Even after recent publications on the subject of eddy conductivities in liquid metal flows many open problems remain. In the paper of Kader & Yaglom /1/ a large number of experimental data are summarized for the Nusselt number Nu, the universal logarithmic temperature profile T^+ and for the turbulent Prandtl number. In the region where both, the velocity and temperature profiles, follow its logarithmic laws, the data show a constant turbulent Prandtl number which depends neither on the wall distance y nor on the molecular Prandtl number Pr. This cannot be used for low Reynolds number flows because there the conductive sublayer extends from the wall to almost the center of the channel. Consequently, no region of a logarithmic temperature profile exists. Reynolds /2/ discusses and classifies 30 different methods for the prediction of turbulent Prandtl numbers. Some methodical problems become evident, for example a missing or wrong functional dependence on wall distance, on molecular Prandtl number, or on Reynolds number. In the work by Dutt /3/ some discrepancies are noted between experimental and theoretically predicted data, but here the experimental data are put in doubt. Thermal contact resistance, incomplete wetting, and longitudinal conduction appear to be the main reasons. This conclusion may be confirmed using the publication by Lawn /4/. He develops a spectral theory to predict turbulent temperature fluctuations in liquid metals. In attempting to check this theory by summarizing experimental data for the turbulent Prandtl number, for the turbulent heat flux, for the rms (root mean square) value of temperature fluctuations and of the cross stream velocity fluctuations, and for the heat flux correlation coefficients, he had to conclude that many of the published data are in error because they show correlation coefficients greater than one.

In this work, the method of direct numerical simulation is used to calculate turbulent liquid metal flows in plane channels and annuli. The method is based on a finite difference formulation of the complete time dependent and three-dimensional mass, momentum, and energy equations for the gross scale part of turbulence. The small scales, which are not directly resolved by the finite difference grid, are represented by special subgrid scale models. Such a method was firstly applied to the momentum transport in channels by Deardorff /5/ for inviscid flows, and by Schumann /6/ for flows at finite Reynolds numbers. The author of this work developed a model which is also applicable for low Reynolds number flows, and which includes heat transport at different Prandtl numbers /7,8/. The subgrid scale model coefficients are calculated by the theory of isotropic turbulence. In the first part of this work those pecularities of the model and of the theory to calculate the coefficients are discussed, which correspond to applications to low Prandtl numbers. Then the model is applied to the simulation of liquid metal flows. It is the purpose of this work to predict statistical data for temperature fluctuations in some exemplary flows by use of the cited method and model. The results can be used instead of experimental data for the development of statistical turbulence models. In contrast to most experimental data, the numerical results confirm the spectral theory of Lawn cited above.

2. Numerical simulation method

In this chapter only a brief description of the principles of the method of direct numerical simulation and of the computer model used is given. The reader, who is interested in more details on the subject of deducing and solving numerically the basic equations is referred to /7,8/.

2.1 Volume averaged basic equations

The method of direct numerical simulation of turbulent flows is based on the complete three-dimensional non-stationary equations for the conservation of mass, momentum and heat. For an application of finite difference schemes these basic equations are transformed to a finite difference form for the mesh cell averaged variables Y (Y any quantity) by formal integration over the volume $V = \Delta x_1 \Delta x_2 \Delta x_3$ of one mesh cell. In case of volume averaging of partial space derivatives the Gaussian theorem leads directly to finite differences $\delta_j {}^j\bar{y}$ for the surface averaged values ${}^j\bar{y}$, where j denotes the normal of the respective mesh cell surface ${}^jF$. The resultant averaged equations for mass, momentum and thermal energy read as follows (for simplicity Cartesian coordinates are used here; application to cylindrical coordinates is shown in /7/):

$$\delta_i \; {}^{i}\bar{u}_i = 0$$

$$\frac{\partial}{\partial t} \; {}^{V}\bar{u}_i = - \delta_j \; {}^{j}\overline{\bar{u}_j \bar{u}_i} - \delta_i \; {}^{i}\bar{p} + \delta_j \left(\frac{1}{Re^*} \; {}^{j}\overline{\frac{\partial u_i}{\partial x_j}} \right) \qquad i=1,2,3 \qquad (1)$$

$$\frac{\partial}{\partial t} \; {}^{V}\bar{T} = - \delta_j \; {}^{j}\overline{\bar{u}_j \bar{T}} + \delta_j \left(\frac{1}{Pe^*} \; {}^{j}\overline{\frac{\partial T}{\partial x_j}} \right) + \dot{Q}$$

The summation convention is used for repeated lower indices. These equations are made dimensionless by means of the channel width D, the friction velocity $\overline{u^*} = \sqrt{\tau_w/\rho}$ (τ_w = time mean wall shear stress averaged over both walls, ρ = constant density), the time scale $t^* = D/\overline{u^*}$, and the heat flux temperature $\overline{T^*} = \dot{q}_w/(\rho \; c_p \; \overline{u^*})$, where $\dot{q}_w$ = time mean wall heat flux, c_p = constant specific heat capacity. Consequently, the Reynolds number is defined as $Re^* = \overline{u^*} \; D/\nu$ (ν = kinematic viscosity), and the Peclet number is defined as $Pe^* = Re^* \; Pr = \overline{u^*} \; D/a$ (a = thermal diffusivity). $\dot{Q}$ is the specific volumetric heat source.

In the computer code TURBIT-2 /7/ applied here the partial derivatives which still remain in eq. (1), and the quantities not defined on the staggered grid used are approximated in a linear second order manner. For time integration an explicit mixed Euler - leap frog scheme is used in combination with Galilean transformations of the mean velocity and temperature fields to maximize the permissible time step widths. The calculation of the pressure field follows the well-known method of solving a Poisson equation by use of the fast Fourier transformation.

The geometries considered in the computer model are infinite plane channels and infinite annuli with different ratios of radii R_1/R_2 (R_1 = radius of inner wall, R_2 = radius of outer wall). The infinity is due to the periodi-

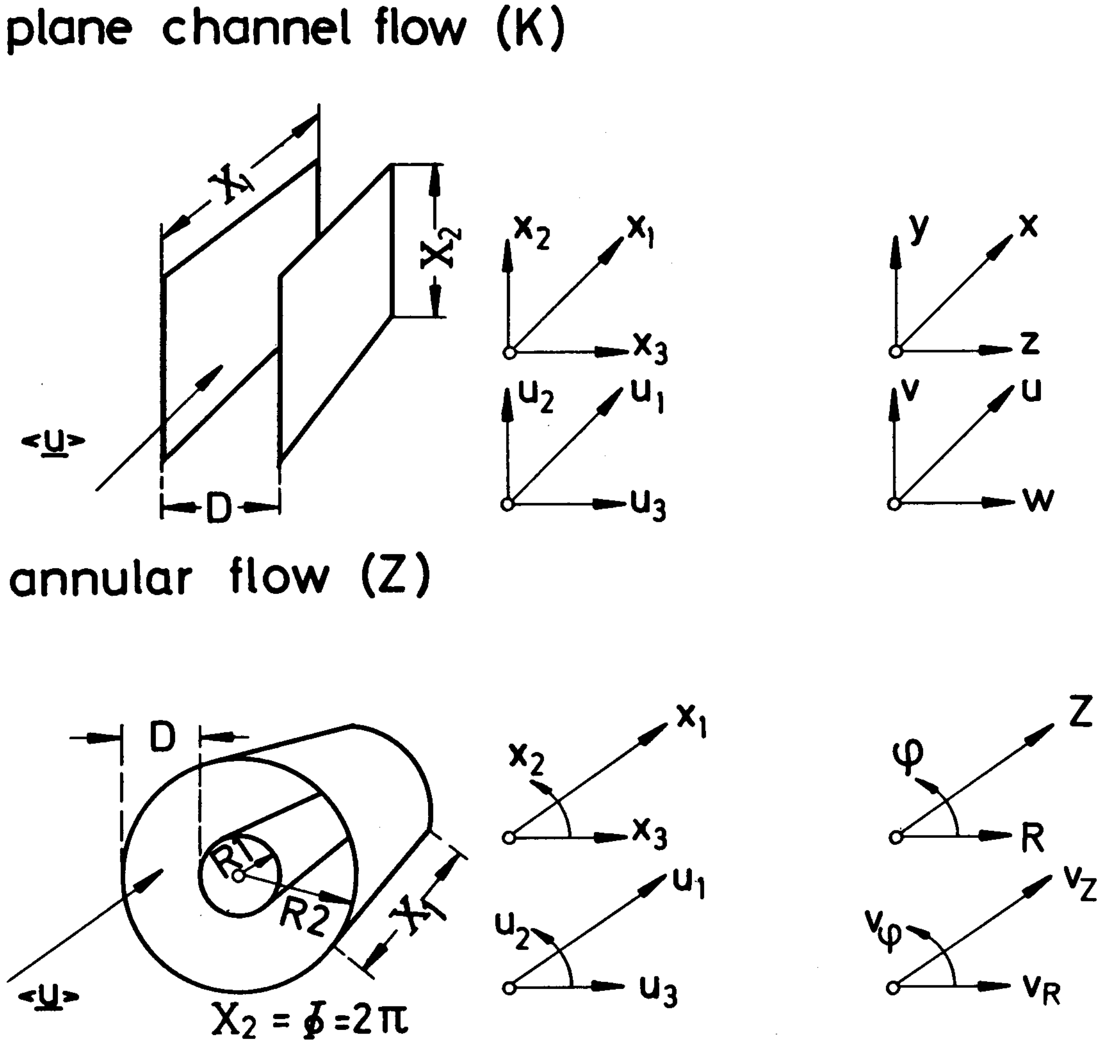

Fig. 1: Channel geometries under consideration. The time mean flow vector $<\underline{u}>$ points in both channels in the x_1-direction.

city in the mean flow direction x_1 and spanwise direction x_2. The periodicity lengths $X_1 = IM\,\Delta x_1$ and $X_2 = JM\,\Delta x_2$ (see Fig. 1) are prescribed via the corresponding numbers of mesh cells IM and JM, and via the respective grid widths Δx_1 and Δx_2. Due to periodicity, axial gradients in the temperature field can not be recorded easily. A possible transformation is given in /7/, but is not used here.

The wall conditions are mostly formulated exactly. An important exception is the wall shear stress $\tau_w = -1/Re^{*}\ {}^3\overline{\partial u_1/\partial x_3}$ and the normal wall heat flux $\dot{q}_w = -1/Pe^{*}\ {}^3\overline{\partial T/\partial x_3}$. In turbulent channel flows with $Pr \geq 0.7$, both gradients show strong changes near the wall which cannot be resolved with the grids used in this work. Therefore these wall fluxes are approximated in a manner which is consistent with the universal velocity and temperature profiles. The method accounts for influences from wall roughness, Reynolds number, Prandtl number, and grid resolution capabilities. For liquid metal flows, no wall functions need to be used for the wall heat flux because of the large spatial extension of the conductive sublayer, which is directly resolved by the grids used. Thus, a valid approximation for the wall heat flux in case of liquid metal flows is

$$\dot{q}_w = -\frac{1}{Pe^{*}}\ {}^3\overline{\frac{\partial T}{\partial x_3}} \sim \frac{-2}{Pe^{*}\,\Delta x_3}\left({}^V\overline{T}_1 - T_w\right) \qquad (2)$$

where ${}^V\overline{T}_1$ is the temperature in the wall adjacent grid cell, and T_w is the wall temperature.

2.2 Subgrid scale heat flux model for liquid metals

The basic equations (1) contain averaged products of velocities and temperature, which cannot be calculated from these equations. In a first step we split the unknown terms by splitting the dependent variables in a large scale part ${}^{j}\overline{Y}$ directly resolved by the grid and in a subgrid scale part Y', which represents the unresolved fluctuating part of $Y = {}^{j}\overline{Y} + Y'$. This results in the still exact equations:

$$
\begin{aligned}
{}^{j}\overline{u_j u_i} &= {}^{j}\overline{u_j}\;{}^{j}\overline{u_i} + {}^{j}\overline{u_j' u_i'} \\
{}^{j}\overline{u_j T} &= {}^{j}\overline{u_j}\;{}^{j}\overline{T} + {}^{j}\overline{u_j' T'}
\end{aligned}
\tag{3}
$$

Only for the subgrid scale parts of the total fluxes model assumptions have to be introduced. The models used in the present code have been described, and extensively tested elsewhere over a wide range of Reynolds numbers, Prandtl numbers, ratios of radii, and space dependent wall roughnesses /7-9/. Therefore, here the discussion is restricted to the strong influence of molecular conduction on the subgrid scale heat flux model in case of liquid metal flows. The model for such flows is the following:

$$
{}^{j}\overline{u_j' T'} = -\,{}^{j}a_t\;\delta_j\,\left({}^{v}\overline{T} - \langle {}^{v}\overline{T} \rangle\right) \tag{4a}
$$

$$
j=1,2,3
$$

$$
{}^{j}a_t = C_{T2}\;{}^{j}C_T\,\left({}^{j}F\;\;{}^{j}\overline{E'}\right)^{1/2} \tag{4b}
$$

This means that we assume gradient diffusion proportional to an effective eddy conductivity ${}^{j}a_t$ and to the local gradient of the temperature fluctuations. The unknown eddy conductivities are modeled by a kind of Prandtl-energy-length-scale model. ${}^{j}F^{1/2}$ is the characteristic length scale. The characteristic energy scale is the subgrid scale kinetic energy ${}^{j}\overline{E'}$ within the area ${}^{j}F$:

$$ {}^{j}\overline{E'} = \frac{1}{2}\ {}^{j}\overline{(u_i - {}^{i}\overline{u_i})^2} \qquad (5)$$

This energy is also needed in the momentum subgrid scale model. It is calculated from an additional conservation equation which is solved simultaneously with eqs. (1). Both scales account for the fact that the subgrid scale heat fluxes are strongly dependent on the spatial resolution capabilities of the grids. The influence of the model correctly tends to zero with increasing spatial resolution.

The factor ${}^{j}C_T$ in eq. (4b) is introduced to correct for geometrical anisotropies of the grid. It depends only on grid parameters and is of order one; in case of isotropic mesh cells ${}^{j}C_T = 1$. The dominating coefficient for our special application is C_{T2}. It has to be determined so that the production of subgrid scale temperature variances caused by this model

$$\text{production} = \langle P_T \rangle = \langle \overline{{}^{j}\overline{u_j' T'}}^{\,j}\ \delta_j\ {}^{j}\overline{T} \rangle \qquad (6)$$

is equal in the statistical mean to its subgrid scale dissipation ${}^{v}\overline{\varepsilon'}_T$:

$$\text{dissipation} = \langle {}^{v}\overline{\varepsilon_T'} \rangle = \langle {}^{v}\overline{\varepsilon_T} \rangle - \langle \frac{1}{Pe^{*}}\ \overline{\delta_j\ {}^{j}\overline{T}}^{\,j}\ \delta_j\ {}^{j}\overline{T} \rangle \qquad (7)$$

These equations are taken from a formally deduced conservation equation for the subgrid scale temperature variances ${}^{v}\overline{E_T'} = 1/2\ {}^{v}\overline{T'^2}$. The overbar $\overline{\quad}^{\,j}$ denotes linear averaging over two in the j direction neighbouring values. From eqs. (4), (6) and (7) we get:

$$C_{T2} = \frac{\langle {}^{v}\overline{\varepsilon_T} \rangle - \langle \frac{1}{Pe^{*}}\ \overline{\delta_j\ {}^{j}\overline{T}}^{\,j}\ \delta_j\ {}^{j}\overline{T} \rangle}{\langle \overline{{}^{j}C_T{}^{2}\ \ {}^{j}F\ \ {}^{j}\overline{E'}}^{\,j} \rangle^{1/2}\ \langle \overline{\delta_j\ {}^{j}\overline{T}}^{\,j}\ \delta_j\ {}^{j}\overline{T} \rangle\ \gamma_T} \qquad (8)$$

The denominator has been split into two parts to replace the triple correlations introducing a correction factor γ_T of order one ($\gamma_T \geq 1$).

We may assume that subgrid scale turbulence, which is mostly associated with high wave numbers in the energy spectra of velocity and temperature fluctuations, is nearly independent on boundary conditions etc. and can therefore be regarded as locally isotropic. So the theory of isotropic turbulence, as given for example in /10/ can be used to calculate all two-point correlations contained in (8) on the basis of the well-known Kolmogorov-spectrum for the total kinetic energy of turbulence E(k) (k = wave number) and on the basis of the Batchelor-spectrum for twice the total energy of temperature fluctuations $E_T(k)$:

$$\begin{aligned} E(k) &= \alpha \quad < \varepsilon >^{2/3} \; k^{-5/3} \\ E_T(k) &= \beta \quad < \varepsilon >^{-1/3} \; < \varepsilon_T > k^{-5/3} \end{aligned} \tag{9}$$

For the constants in the spectra we use $\alpha = 1.5$ and $\beta = 1.3$ determined in a literature review. The complete theory to calculate all terms contained in (8), and similarly for ${}^jC_T$, is very extensive and complicated. In the following schematic result, the functions $f_i(\Delta x_j)$, which have to be evaluated by numerical integration, are of order one and depend only on grid parameters. The dissipation ε_T of temperature variances cancels out

$$C_{T2} = \frac{1 - \beta \, f_1(\Delta x_i) \, Pe^{*-1} \, V^{-4/9} <\varepsilon>^{-1/3}}{\gamma_T \, \beta \, \alpha^{1/2} \, f_2(\Delta x_i)} \tag{10}$$

The second terms of the numerators of (8) and (10) represent the dissipation in the directly resolved temperature field. For large Peclet numbers and coarse grids it may be neglected. In such cases C_{T2} is dominated by the denominator and can be calculated without any further empirical input data.

The second term of the numerator of eq. (10) become only in those cases important in which the Peclet number and mesh cell volume is small. That means that in all cases, in which the turbulent temperature fluctuations are almost totally contained in the directly resolved large scale structure, the coefficient C_{T2}, and with it the total subgrid scale heat flux model, tends to zero as expected. In this transition range of the model the unknown dissipation $<\varepsilon>$ has to be calculated in addition. A useful approximation for turbulent channel flow purposes is deduced from the assumption of equality of production $= - < u_1'u_3' > \partial< u_1 > / \partial x_3$, and dissipation of kinetic energy, wherein the total turbulent shear stress $< u_1'u_3' >$ is calculated by use of the Prandtl mixing length model, and the velocity gradient by use of the universal logarithmic velocity profile. This results in:

$$< \varepsilon > = (\kappa y)^2 \left| \frac{\partial<u_1>}{\partial x_3} \right|^3 = \frac{1}{|\kappa \; y|} \qquad (11)$$

We use $\kappa = 0.4$ for the Karman constant. By eq. (11) the subgrid scale coefficient C_{T2} (eq. 10) becomes, in addition to the dependence on the grid parameters, dependent on the wall distance y. In accordance with the higher turbulent temperature fluctuations near the wall, and the corresponding larger extension of the spectra of the temperature fluctuations to higher wave numbers, the model shows increasing values of C_{T2} for decreasing wall distance.

A numerical evaluation of eqs. (8 to 11) is shown in Fig. 2 for an equidistant Cartesian grid with $\Delta x_1 = \Delta x_2 = 1/8$ and $\Delta x_3 = 1/16$, denoted later

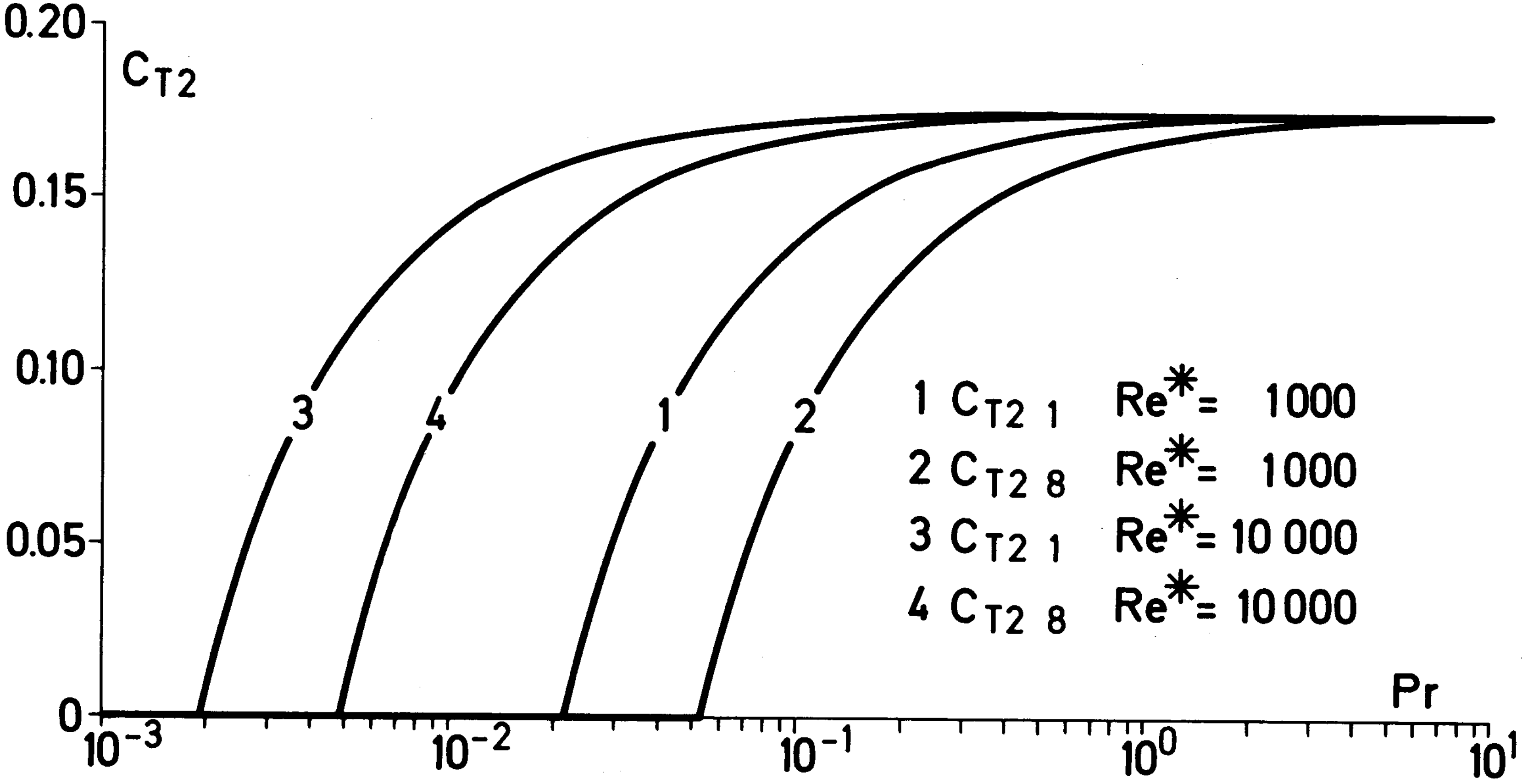

Fig. 2: The calculated subgrid scale coefficient C_{T2} (γ_T=1.0) for grid K7 as a function of the Prandtl number. The parameters are the shear velocity Reynolds number and the mesh index K in the x_3-direction (y(K=1)=0.0313 = wall adjacent mesh, y(K=8)=0.469= center adjacent mesh)

on as grid K7. For very low Prandtl and Reynolds numbers C_{T2} is zero. For increasing Prandtl numbers a transition range follows in which C_{T2} increases with increasing Prandtl and Reynolds numbers, and with decreasing wall distance. For Prandtl numbers greater one C_{T2} gets independent of all parameters for the coarse grid under consideration. In this region the conductive sublayer is no longer resolved by the grid; consequently, no influence of Pe^* is found in the subgrid scale heat flux model.

The correction factor $\gamma_T \geq 1$ included in eq. (8) has to be determined numero-empirically. It was tried in /7,8/ to adjust γ_T by using the complete heat flux model, as is used for $Pr > 0.1$, together with the coarse grid K7, for the simulation of a high Reynolds number flow with $Pr = 0.7$; this is a case in which the subgrid scale heat flux model should be important. Nevertheless, γ_T showed very weak influences only. Obviously, the resolution capabilities of the grids with this Prandtl number are better for temperature fluctuations than for velocity fluctuations. Indeed, the recent publication by Hishida & Nagano /11/ shows in the temperature fields relatively more energy associated with low wave numbers than in the velocity field, and vice versa with high wave numbers. Therefore, and due to the wide scatter of experimental data, we could not adjust γ_T. In order to use an unchanged turbulent subgrid scale Prandtl number, the same value $\gamma_T = 1.4$ was chosen as in the subgrid scale model for the momentum fluxes.

The high insensitivity to changes in γ_T is even more pronounced for lower Prandtl numbers. In Fig. 3 some results for five simulations of the flow of liquid sodium with different γ_T are shown . Theoretically, one expects $\gamma_T \geq 1$. For this region approximately no influence can be detected although γ_T extends over two orders of magnitude and although the coefficients C_{T2} are only in the inner third of the channel equal to zero. Thus, nothing contradicts to use the same value of γ_T for all Prandtl numbers under consideration.

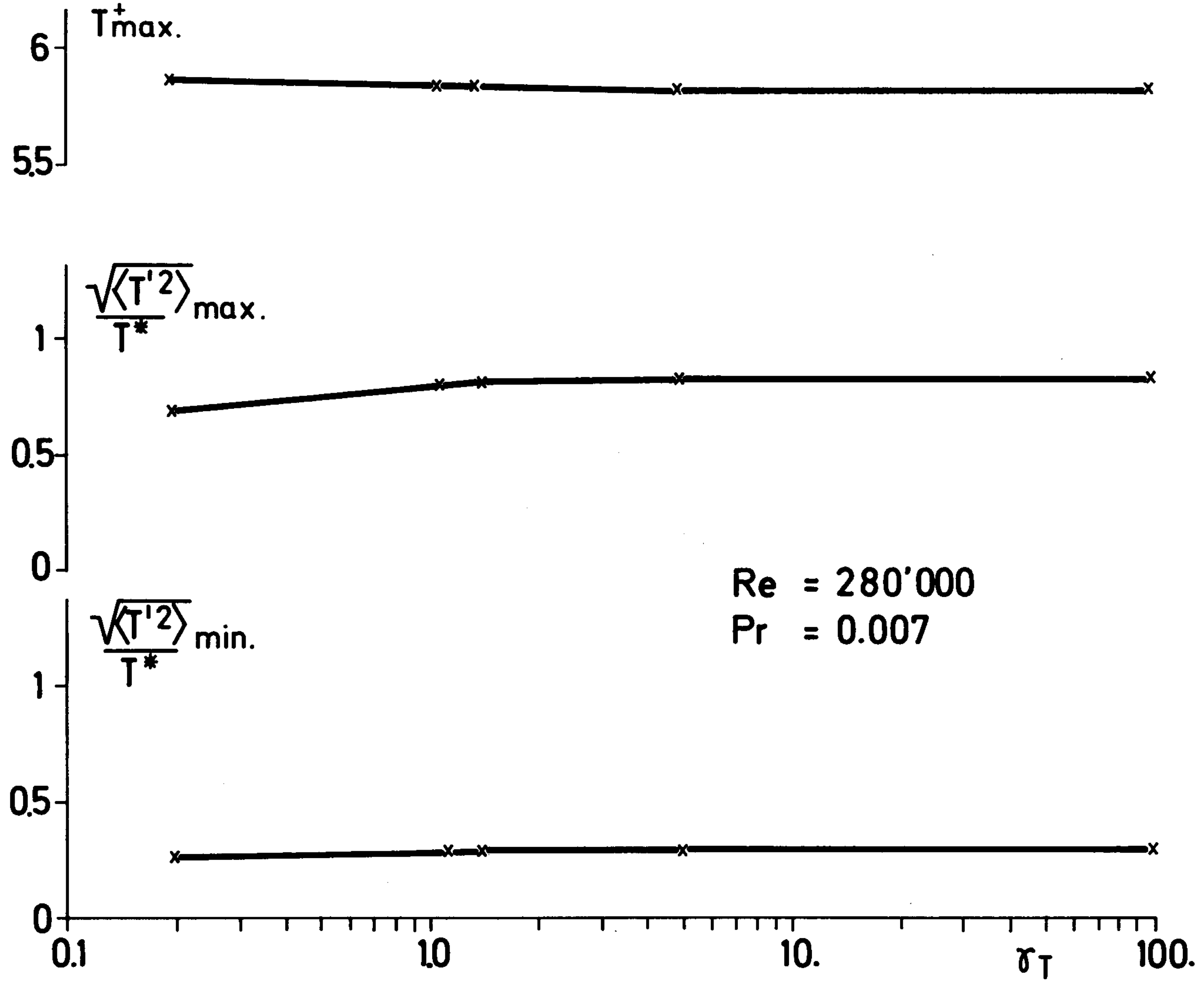

Fig. 3: Insensitivity of statistical data of turbulent temperature fluctuations to changes of the correction factor γ_T of the subgrid scale heat flux coefficient, grid K7. $T^+ = T/T^*$; max. and min. are taken from the lateral profiles.

3. Case specifications and initial conditions

The specifications of the cases under consideration have been compiled in Tab. 1. For the Prandtl number of liquid sodium under reactor conditions, Pr = 0.007, several calculations with different arbitrarily chosen Reynolds numbers have been carried out for a plane channel and an annulus. The resulting Reynolds number Re is linked to Re^* prescribed, to the channel average of the calculated mean velocity $^V\!< u_1 >$, and to the friction coefficient c_f:

$$Re^* = Re/(2\ {}^V\!\langle u_1\rangle) = Re/2\sqrt{c_f/8} \qquad (12)$$

The calculations for the flow of liquid mercury in an annulus, Pr = 0.0214, refer to the experiments by Dwyer et al. /12/. The calculations for air, Pr = 0.7(1), have been added to show the steadiness of numerical results.

The thermal boundary conditions for the annuli are comparable to those of most experiments. We use adiabatic outer walls and by prescribed uniform wall heat fluxes heated inner walls. The plane channel flows of sodium are heated by volumetrical heat sources within the fluid, and cooled at the walls by prescribing equal wall temperatures. By this type of boundary conditions the temperature profiles in the plane channels become directly comparable to the profiles in uniformly cooled or heated pipes. The plane channel flow of air is cooled at wall w1 by prescribing a constant wall temperature, and heated at wall w2 by a constant heat flux.

The parameters of the finite difference grids used are listed in Tab. 2. The Cartesian grids K use 2048 or 8192 mesh cells; the cylindrical grids Z use 4096 or 16384 mesh cells. The periodicity lengths Φ chosen for the circumferential direction in the annuli allow to record a quarter or a half of the

Tab. 1: Case Specifications. The grid specifications follow Tab. 2

Pr	Re	Pe	R_1/R_2	grid	thermal boundary conditions	$\dot{Q}$
.007	46 000	322	.25	Z9	$\dot{q}_{w1}=1$, $\dot{q}_{w2}=0$	0
	50 000	350	1.	K2.2	$T_{w1}=T_{w2}=0$	2
	100 000	700	.25	Z2.2	$\dot{q}_{w1}=1$, $\dot{q}_{w2}=0$	0
	280 000	1 960	1.	K7	$T_{w1}=T_{w2}=0$	2
.0214	100 000	2 140	.479	Z2.2	$\dot{q}_{w1}=1$, $\dot{q}_{w2}=0$	0
	145 300	3 110	.479	Z2.2	$\dot{q}_{w1}=1$, $\dot{q}_{w2}=0$	0
.7	50 000	35 000	.25	Z2.2	$\dot{q}_{w1}=1$, $\dot{q}_{w2}=0$	0
.71	50 000	35 500	1.	K2.2	$T_{w1}=0$, $\dot{q}_{w2}=-1$	0

Tab. 2: Grid specifications and typical computing times. IM, JM and KM denote the number of mesh cells in the three space directions

Grid Specifications	K7	K2.2	Z9	Z2.2
IM (x_1, Z)	16	32	16	32
JM (x_2, φ)	8	16	16	32
KM (x_3, R)	16	16	16	16
X_1	2	3.2	2	3.2
X_2, Φ	1	2	$\pi/2$	π
no. of time steps	2690	1875	3080	2625
CPU-time, IBM 370/168	47 min	2.5 h	2 h	7 h

channel, which seems to be appropriate for the ratios of radii under consideration /7/. The assignment of the given equidistant but not equally sided grids to the several cases is given in Tab. 1.

The radial profiles of all coefficients of the total subgrid scale model have to be calculated. For example using the complete theory indicated in eqs. (8 to 11) to calculate the coefficient C_{T2} leads to the results listed in Tab. 3. For the three cases with the lowest Peclet numbers Pe = Re Pr the coefficient is zero everywhere in the channels. This means, no subgrid scale heat flux model is necessary in these cases. As expected from Fig. 2 for increasing Peclet numbers C_{T2} becomes non-zero predominantly near the walls, in the annuli especially near the outer walls. For the two highest Peclet numbers the subgrid scale heat flux coefficient is approximately constant all over the channels. For these two cases the complete subgrid scale heat flux model has been used as given in /7,8/, whereas the simpler model, given in eq. (4) has been used for all liquid metal flows.

To start the numerical time integration of eqs. (1), three dimensional initial data for the three velocity components and for the temperature are required. In principle, nearly arbitrary data can be used; but in order to shorten the computer time necessary to reach a fully developed flow the statistical properties of the initial fields should be very near to those of fully developed flow. Therefore, we use the universal logarithmic laws for the mean of u_1 and T and zero for the mean of u_2 and u_3. By use of a pseudo random number generator these mean values are superimposed by random fluctuations with amplitudes corresponding to the expected rms-value profiles. Better initial data have been deduced for the case with Pe = 350, which uses the unchanged numerical results for the velocity fields of the case with Pe = 35 500.

Tab. 3: Results for the subgrid scale coefficient $C_{T2}(K)$ for mesh cell no K=1 near wall w_1, for K=8 near the center of the channel, and for K=KM near wall w_2. The calculated values are divided by $\gamma_T=1.4$

Pr	Pe	grid	$C_{T2}(1)$	$C_{T2}(8)$	$C_{T2}(KM)$	$C_{T2}=0$ for $(R-R_1)/(R_2-R_1)$
.007	322	Z9	0.	0.	0.	0. - 1.
	350	K2.2	0.	0.	0.	0. - 1.
	700	Z2.2	0.	0.	0.	0. - 1.
	1 960	K7	0.067	0.	0.067	0.31 - 0.69
.0214	2 140	Z2.2	0.065	0.	0.079	0.44 - 0.5
	3 110	Z2.2	0.081	0.030	0.090	-
.7	35 000	Z2.2	0.118	0.118	0.123	-
.71	35 500	K2.2	0.123	0.118	0.123	-

4. Numerical results

Typical computing times for an IBM 370/168 and numbers of time steps NT needed to reach fully developed flow and an additional time interval Δt_{av} for evaluation are given for each grid in Tab. 2, and for each case in Tab. 4. A typical computing time per mesh cell and time step is 580 μsec. Comparing this time to those of simulations without any subgrid scale model with nearly the same code /13/ shows only a 30 % enlargement of the computing time by the subgrid scale models. The channel lengths l covered are in all cases greater than 50 channel widths, and are, therefore, sufficient to reach fully developed flow.

4.1 Phenomenological results

Contourline plots of the resolved instantaneous turbulent temperature fluctuations are shown in Fig. 4 for different annular flows with different molecular Prandtl numbers. The isolines of all of the three cases show larger temperature fluctuations near the lower heated wall than near the upper adiabatic wall. With increasing Prandtl number the amplitude of the fluctuations increases, and the location of its maximum moves nearer to the wall. The patterns show a predominant inclination from the walls in the direction Z of the mean velocity to the center of the channel. The spatial extension of these structures decreases with increasing Prandtl number. In case of liquid sodium only very few small scale structures appear, the dominant structures are much more spatially extended than the typical grid width. For this simulation of liquid sodium flow it appears that the most important part of the temperature fluctuations is contained in the directly resolved field and that the subgrid scale part is of negligible importance. This behaviour is in accordance with the numerical results for the subgrid scale coefficients.

Tab. 4: The realized time intervals t with NT time steps, the resulting channel mean velocities, the covered channel lengths 1, the resulting wall shear stresses, the distances y from wall w_1 of the zero turbulent shear stress, the friction factors c_f, and the number of time steps ΔNT_{av} within the final time intervals Δt_{av} used for time averaging of the given results.

Pe	t	NT	$\frac{v_{\langle u_1\rangle}}{u^*}$	$\frac{1}{D}$	$\frac{u_1^*}{u^*}$	$\frac{u_2^*}{u^*}$	$y(\tau=0)$	c_f	ΔNT_{av}	Δt_{av}
322	3.16	3080	19.19	60.6	1.063	0.984	0.376	0.0217	28	1.16
350	8.24*	4225	19.36	159.5	1.0	1.0	0.5	0.0213	23	2.02
700	3.57	3875	20.93	74.7	1.072	0.981	0.376	0.0183	43	1.25
1960	6.97	2690	23.25	162.1	1.0	1.0	0.5	0.0148	21	2.69
2140	5.21	2450	20.88	108.8	1.037	0.982	0.432	0.0183	32	2.34
3110	20.4	9450	22.43	457.6	1.049	0.976	0.448	0.0159	30	3.24
35000	4.51	2625	19.61	88.4	1.071	0.981	0.376	0.0208	27	1.71
35500	4.00	1875	19.47	77.9	1.0	1.0	0.5	0.0211	22	1.56

* Restarted from case Pe=35500 at t=4.0 after initializing a new temperature field

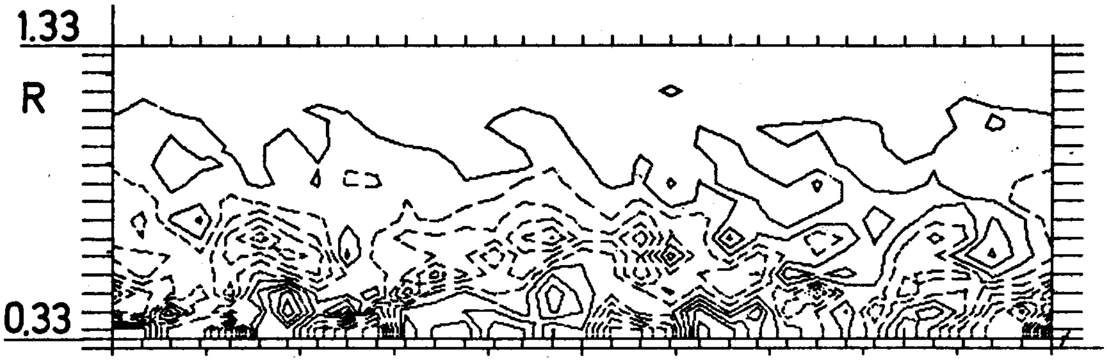

$T'(t = 4.509, \varphi = \pi/8)$ $Re = 50\,000$, $Pr = 0.7$, $R_1/R_2 = 0.25$
$\Delta = 0.5$

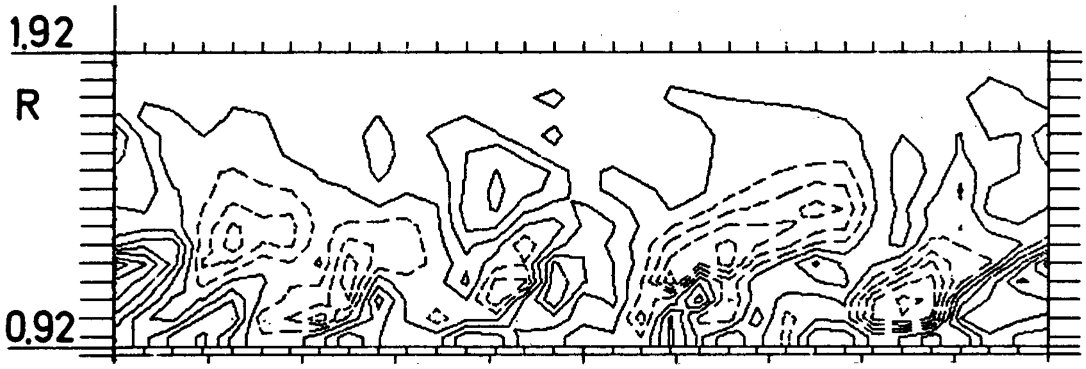

$T'(t = 5.207, \varphi = \pi/8)$ $Re = 100\,000$, $Pr = 0.0214$,
$R_1/R_2 = 0.479$, $\Delta = 0.4$

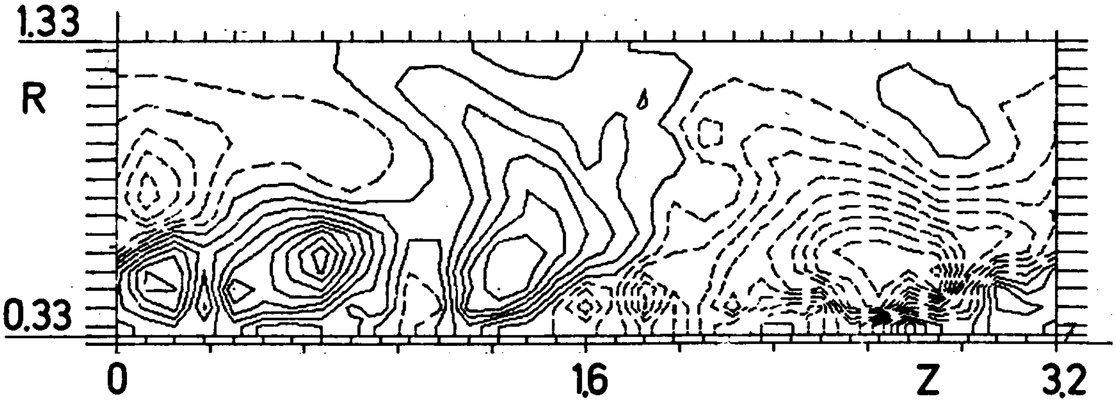

$T'(t = 3.572, \varphi = \pi/8)$ $Re = 100\,000$, $Pr = 0.007$,
$R_1/R_2 = 0.25$, $\Delta = 0.075$

Fig. 4: Contour line plots of the instantaneous resolved temperature fluctuations $T' = T - \langle T \rangle$ for annular flow of air, mercury, and liquid sodium. Sections along the mean flow direction Z. Δ = contour line increment. Dashed lines correspond to negative values.

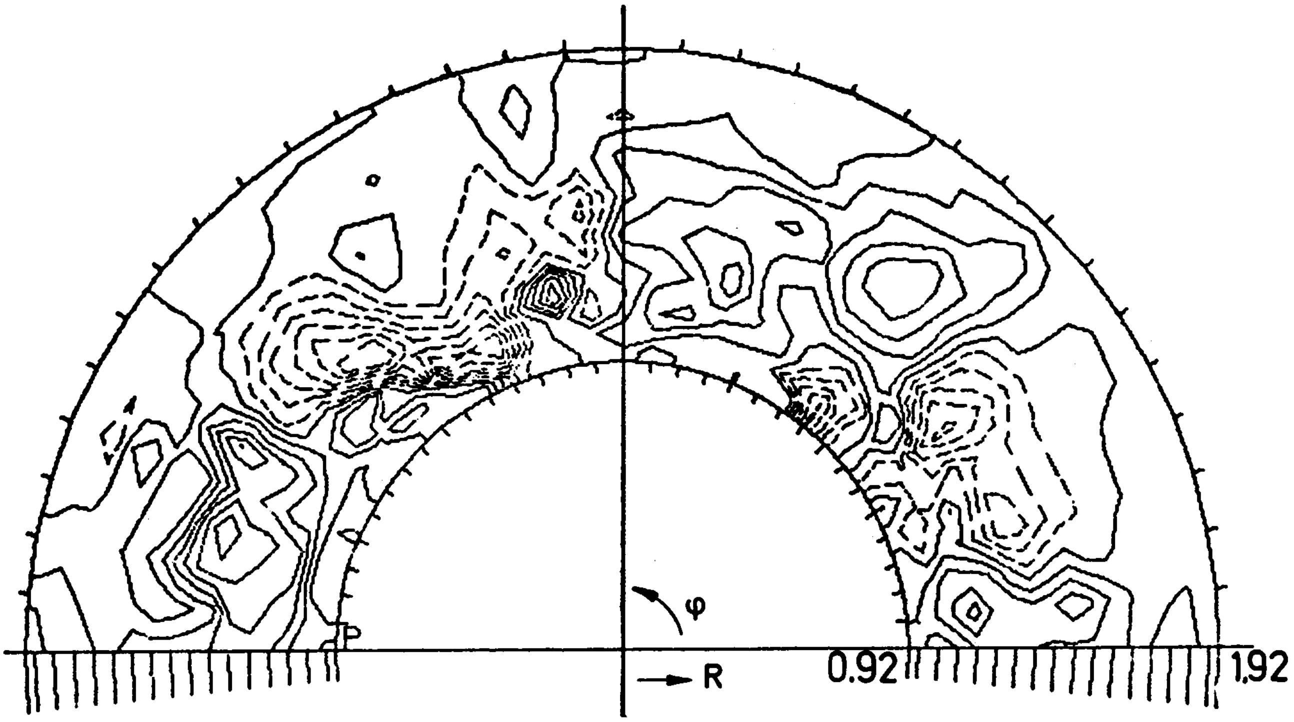

$T'(t = 5.207,\ x_1 = 0.4)$ $Re = 100\,000$, $Pr = 0.0214$,
$R_1/R_2 = 0.479$, $\Delta = 0.4$

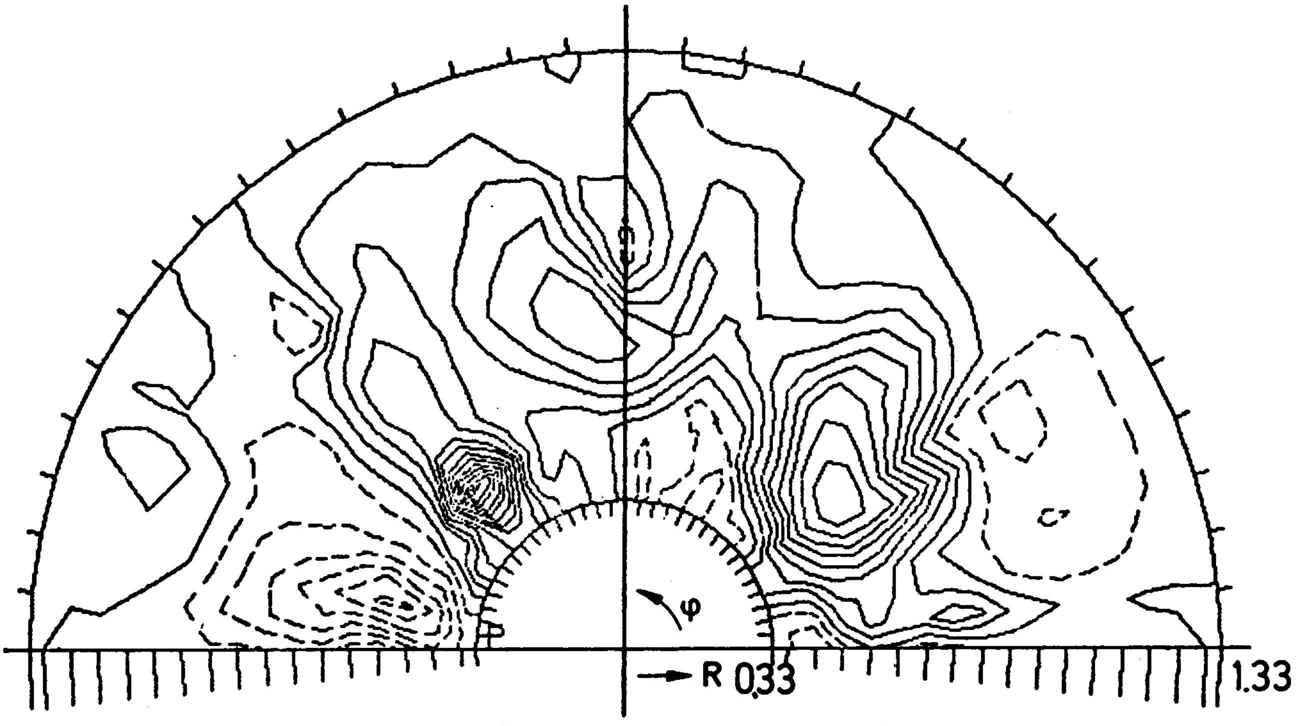

$T'(t = 3.572,\ x_1 = 0.4)$ $Re = 100\,000$, $Pr = 0.007$,
$R_1/R_2 = 0.25$, $\Delta = 0.075$

Fig. 5: Contour line plots of the instantaneous resolved temperature fluctuations for annular flow of mercury and liquid sodium. Sections perpendicular to the mean flow direction.

The same behaviour can equally be detected in cross sections perpendicular to the mean flow direction (Fig. 5). In addition, the section for the liquid mercury case seems to show predominant large scale structures in the center of the channel, whereas the scales are smaller near the heated wall. Thus we find temperature fluctuations with higher wave numbers in the main productive region near the heated wall, and with lower wave numbers in the inner part of the channel where the mean temperature gradient is smaller. This qualitative result agrees with the importance of the temperature subgrid scale model as given by the theoretical result for C_{T2} in Tab. 3.

4.2 Profiles of temperature statistics

For the quantitative evaluation of the time dependent numerical results mean values are taken as averages over planes parallel to the walls. This is possible due to the periodic boundary conditions along these planes. In addition these mean values have been averaged over 21 to 43 different time steps, which are equidistantly distributed within the final time intervals Δt_{av} (Tab. 4). In the same table some results calculated from the velocity fields are included, which will be used here for normalization purposes. Moreover, these data allow the interested reader to judge on the quality of the calculated velocity fields. No verification of the calculated velocity and pressure fields will be given in this work. Those results, which do not depend on the molecular Prandtl number, have been verified in /7 to 9/.

Cross stream profiles of temperature statistics evaluated from the plane channel flow simulations of liquid sodium are given in Fig. 6. In correspondence to the prescribed boundary conditions all profiles are more or less symmetric to the center of the channel. The typical relative standard deviation tsd is between 0.5 % and 7 % for the directly evaluated temperature rms values and heat

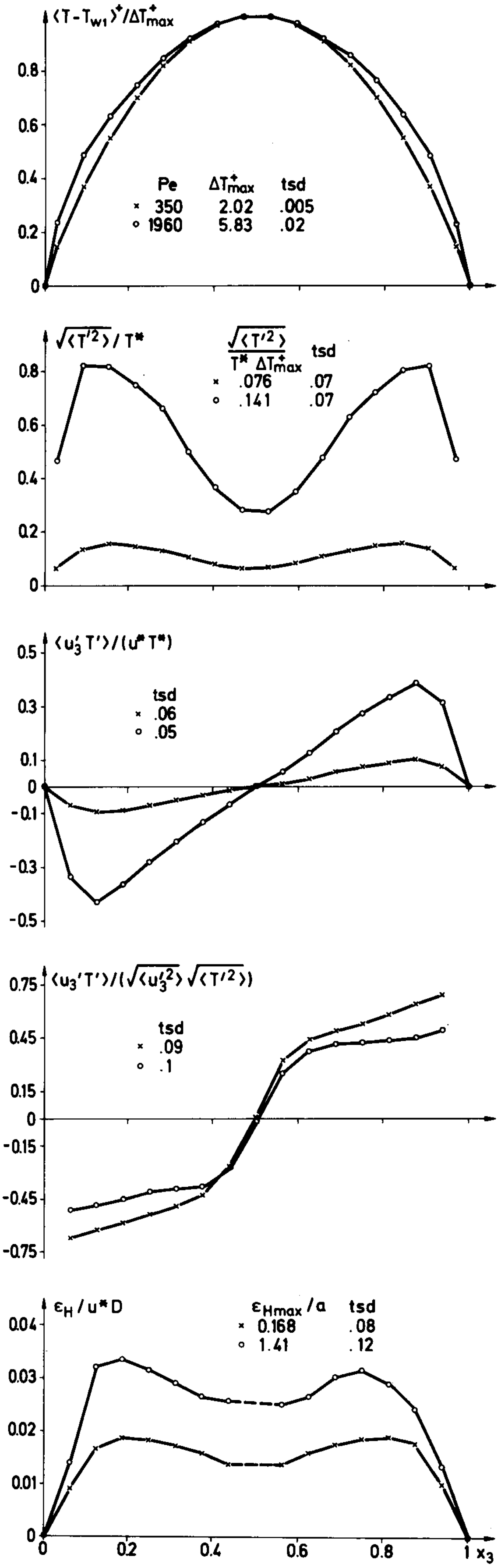

Fig. 6:

Cross stream profiles of temperature statistics for plane channel flows of liquid sodium. From top to bottom: time mean temperatures normalized by the respective maximum temperature differences ΔT^{+}_{max} within the channel; large scale part of the rms-temperature values and their normalized maximum values; large scale part of the cross stream turbulent heat flux; heat flux correlation coefficient; eddy diffusivities for heat and their normalized maximum values. tsd = typical relative standard deviation.

fluxes, and between 8 % and 12 % for the heat flux correlation coefficients and the eddy diffusivities for heat, which are both by definition composed of different single results. The nearly parabolic temperature profiles are typical for most conduction controlled flows. With increasing Reynolds or Peclet number the importance of turbulence increases and, therefore, the gradient near the wall becomes steeper. Accordingly, the rms values of the turbulent temperature fluctuations become higher and the positions of the maxima move nearer to the wall. The turbulent heat flux $<u_3'T'>$ is also higher for the larger Reynolds number. The turbulent heat flux correlation coefficient shows nearly constant values in the outer parts of the channel with the higher Peclet number. In case of the lower Peclet number no constant region is indicated. The absolute value of the correlation coefficient increases by approaching the walls. The eddy diffusivity for heat shows increasing tendency with increasing Reynolds number. Their maximum values, normalized by the thermal diffusivity a, confirm the very low contribution of the turbulent heat flux to the total one in case of the lower Peclet number flow. Thus, both cases may be attributed to the transition range from molecular to turbulent heat transfer.

The results of the evaluation of the annular flow simulations are contained in Fig. 7. All profiles tend to zero near to the adiabatic outer wall: the radial gradients of the temperature profiles are zero near the outer wall; the rms temperature values, as well as the turbulent radial heat fluxes tend to zero there; the radial heat flux correlation coefficients behave similarly, but there seems to be an indication for two approximately constant regions with different heights in the inner and outer halfs of the channels. Again, the correlation coefficients for the lower Peclet numbers show a pronounced increase near the heated wall. The eddy diffusivity profiles are obviously not affected by the special thermal boundary conditions. The profiles show

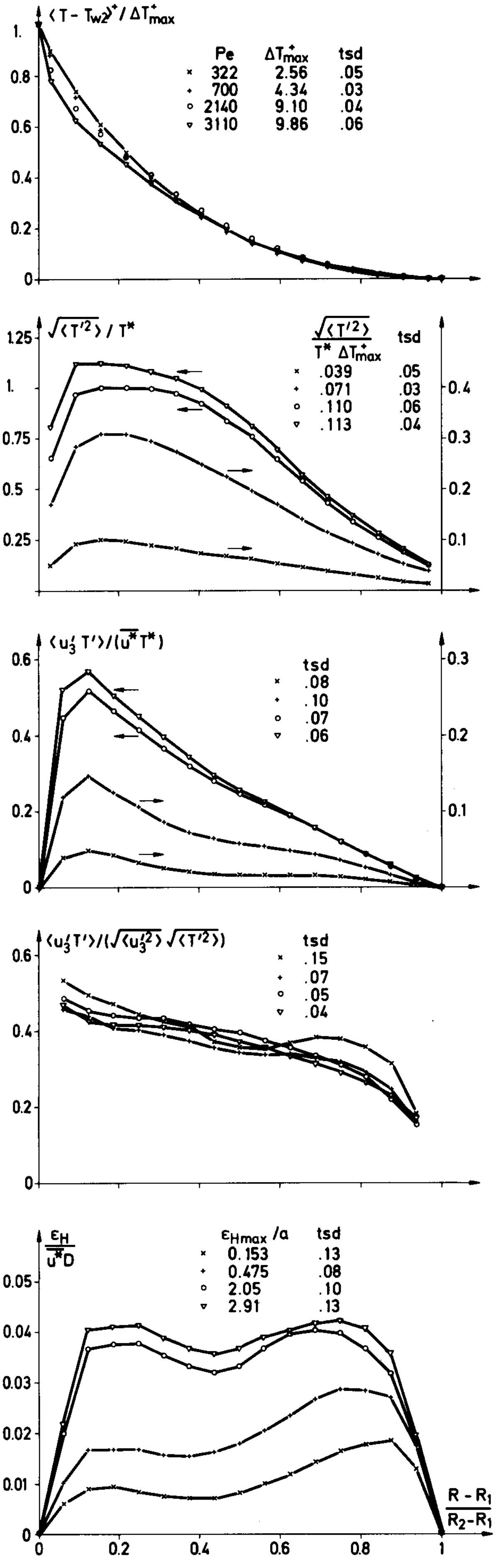

Fig. 7:

Radial profiles of temperature statistics for annular flows of liquid sodium and liquid mercury. From top to bottom: time mean temperatures normalized by the respective maximum temperature differences ΔT^{+}_{max} within the channel; rms temperature values and their normalized maximum values; large scale part of the cross stream turbulent heat flux; heat flux correlation coefficient; eddy diffusivities for heat and their normalized maximum values.

higher peaks near the outer wall, especially in case of the small ratios of radii of both low Peclet number flows. The high Peclet number profiles are not very different. One may conclude that these results are near to the limiting profile for high Reynolds number flow of liquid mercury.

In addition to these evaluations of the numerical time and space dependent results a lot of evaluations of other correlations are possible, predominantly those which are mainly governed by the resolved large scale structure of turbulence. Some examples included in /7/ are the temperature-temperature, the energy-temperature, and the pressure-temperature cross correlations. A complete plot-output from the computer code is given in the Appendix for the annular flow with Pe = 700.

5. Discussion of numerical results

To get an integral judgement on the simulated temperature fields we compare in Fig. 8 the evaluated Nusselt numbers with some empirical formulations from the literature /14-18/. The numerical data of the plane channels, which have two non-adiabatic walls, are in accordance with the respective formulae by Gräber /14/ and Dwyer /15/. For the annular flows with adiabatic outer walls, the empirical data scatter largely, partly depending on the molecular Prandtl number and on the ratio of radii. Only the correlation by Barthels /18/ follows the numerical results for liquid mercury. The numerical results for liquid sodium flows, which are for a ratio of radii of 0.25, are below most results of the formulae. The only curve, which follows all numerical annular flow results, but which gives slightly lower Nusselt numbers, is the curve by Gräber for a plane channel with one adiabatic wall. The large discrepancies with the empirical curves seem to be due to the problems with formulating even radial eddy diffusivity profiles for annular channel flows, whereas in case of plane channel flows, no comparable difficulties appear because the eddy diffusivity and eddy conductivity profiles may be approxi-

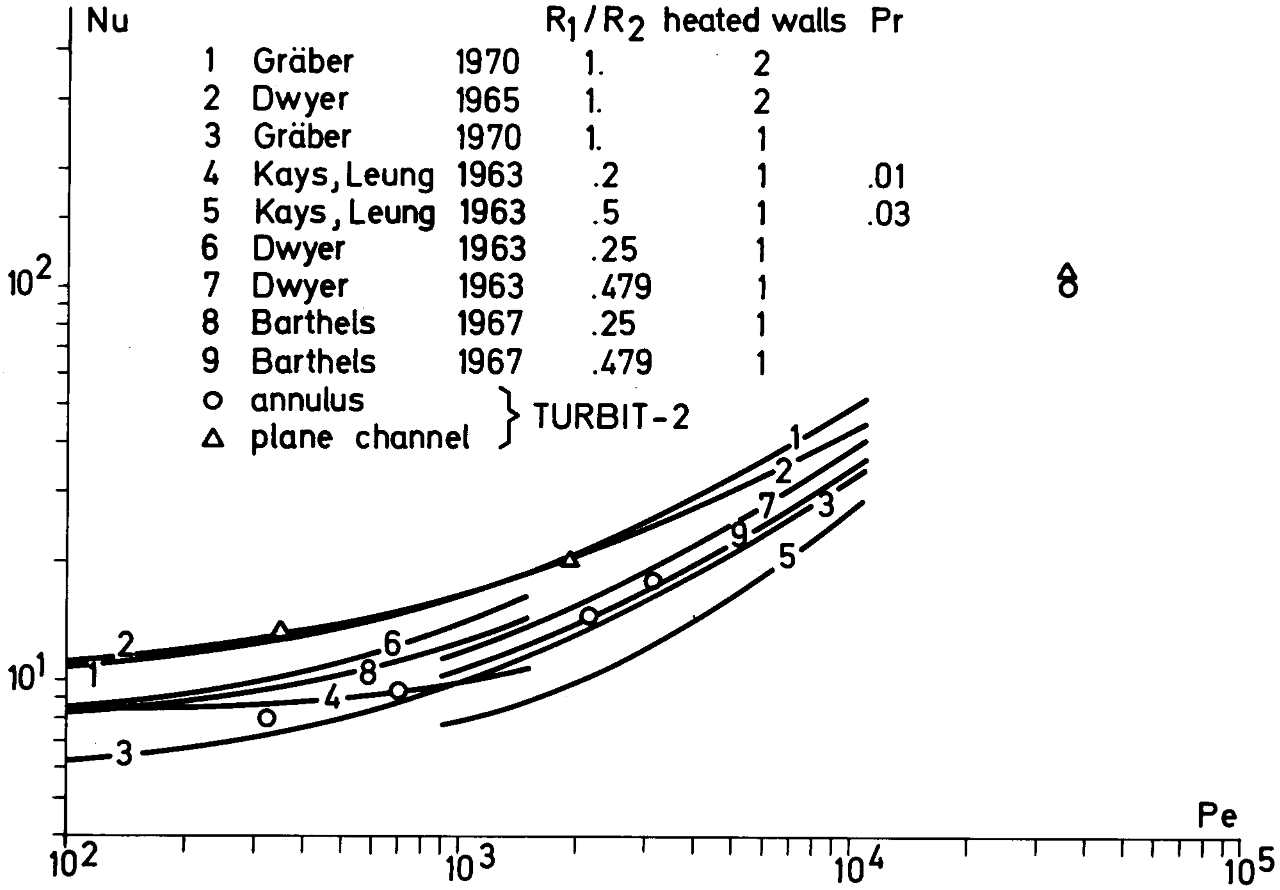

Fig. 8: Comparison of Nusselt numbers Nu = $(\dot{q}_{conv} + \dot{q}_{cond})/\dot{q}_{cond}$ evaluated from the numerical results to empirical formulations. Where necessary, a turbulent Prandtl number of ${}^{v}\langle Pr_t \rangle = 1$ has been used for plotting the empirical curves.

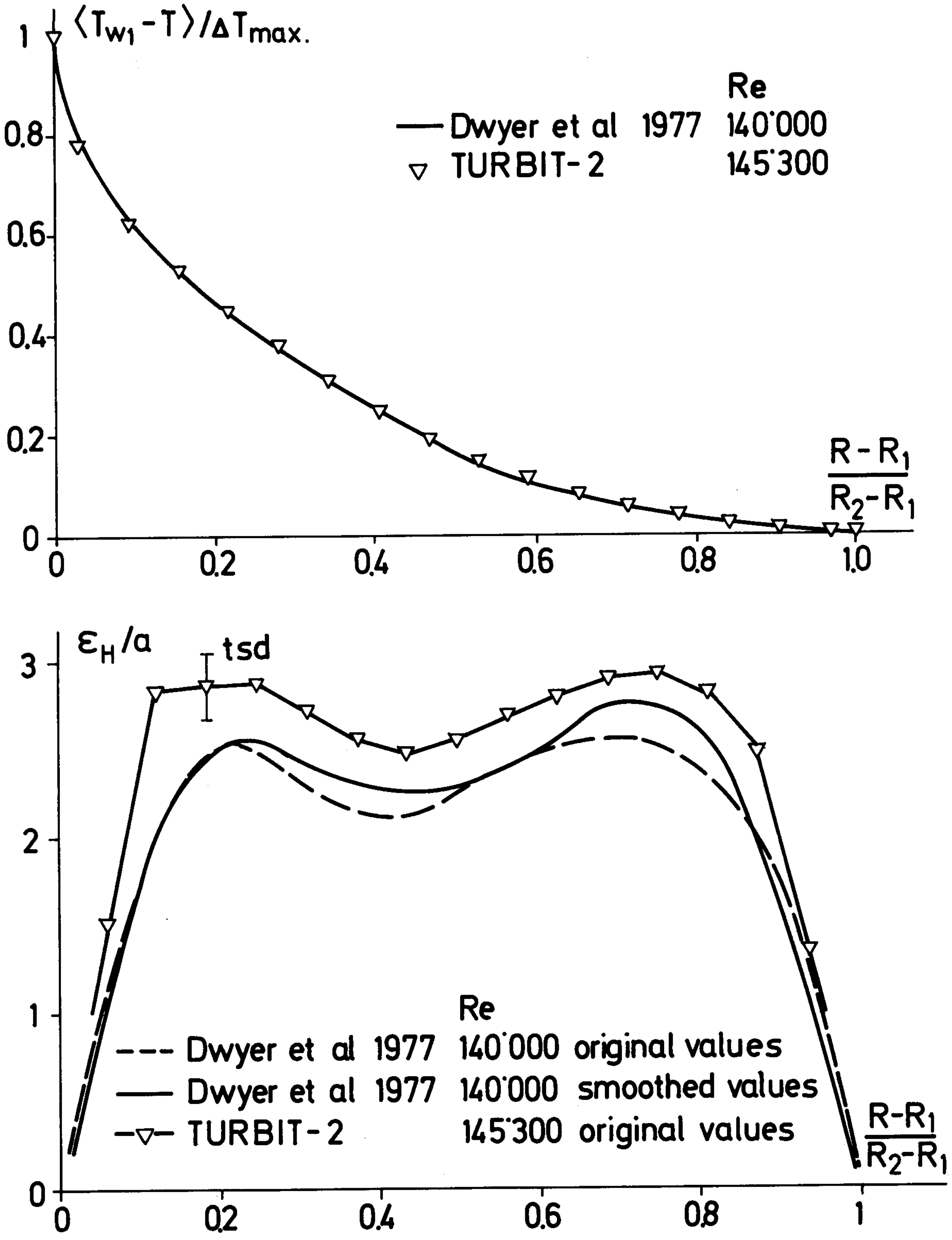

Fig. 9: Temperature- and eddy conductivity profiles evaluated from the numerical simulation, case Pe = 3110, compared to the measured and deduced annular flow data by Dwyer et al. /12/.

mated by using the direct analogy to the better investigated pipe flows.

A more detailed comparison of the numerical results to temperature profiles measured by Dwyer et al. /12/ in an annular channel is given in Fig. 9. Both results are nearly identical. The numerical annular flow results are also confirmed by comparing the eddy conductivity profiles. The numerical results are somewhat higher than the original and smoothed data, calculated by Dwyer et al. from the measured temperature profile. This difference is due to the somewhat higher Reynolds number resulting in the numerical simulation. The typical standard deviation indicates comparable uncertainties of the numerical and experimental results.

Some further results for the eddy conductivity for the other Peclet numbers have been plotted over the Peclet number in Fig. 10. The plane channel data follow in the chosen log-log-presentation a single straight line independent on the Reynolds and Prandtl number. The line is parallel to that through the experimental pipe data by Fuchs /19/. The distance between both lines corresponds to a difference in Peclet number by approximately a factor of two. The difference comes from the different numbers of thermal boundary layers in both channels. The data of the annular flows follow none of these lines: The eddy conductivity for the sodium flows with $R_1/R_2 = 0.25$ increases steeper with increasing Peclet number than the plane channel data, and for the mercury flows with $R_1/R_2 = 0.479$ somewhat flatter. The numerical results for the mercury flows follow nearly exactly the smoothed experimental data by Dwyer et al. /12/. The eddy conductivities in the outer halfs of the channels are for both fluids higher than in the inner halfs. The difference between both values vanishes when the ratio of radii approaches one. These results give an impression on the rather complicated influence of the Reynolds number, Prandtl number, of the ratio of radii, and of thermal boundary conditions on the eddy conductivity.

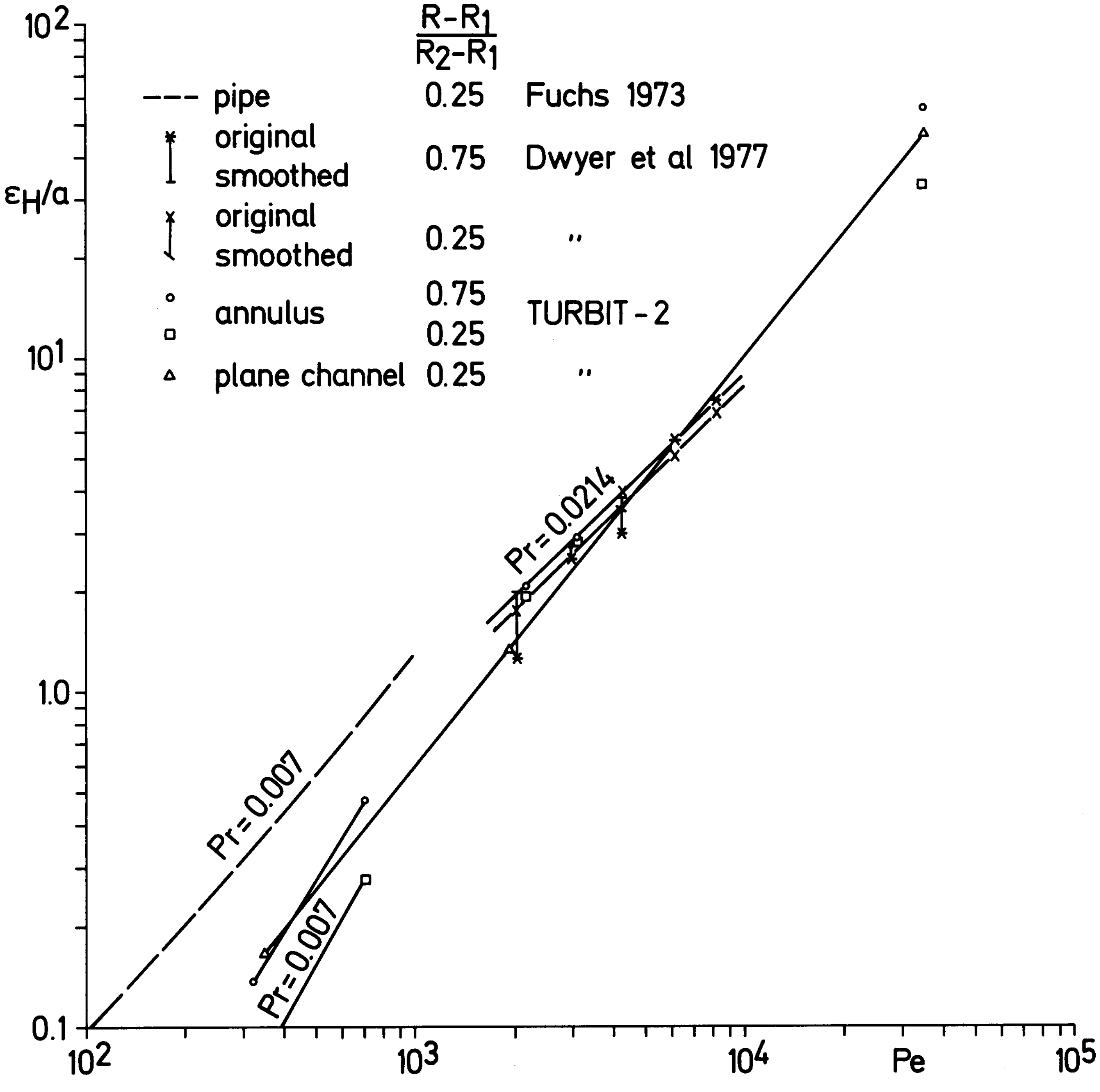

Fig. 10: The influence of the Peclet number on the eddy conductivity normalized by the thermal diffusivity. The data are for the centers of the inner and outer halfs of the channels.

Similar pointwise support can be given to the development of those statistical turbulence models which use additional transport equations for some of the unknown turbulence quantities. As an example the maxima of the radial temperature rms-value profiles are plotted in Fig. 11 over the Peclet number. The qualitative behaviour is largely comparable to that of the eddy conductivity. One important difference becomes evident from the air flow results, which lie far away from the connection lines of the other numerical results. The experimental pipe data for air included in the figure let us assume that for constant Prandtl numbers the rms values at large Peclet numbers does not depend on the Reynolds number. At medium and low Peclet numbers the rms-values seem to depend mainly on the Peclet number but not on the Prandtl number. Further influences come for all cases also from the ratio of radii and from the thermal boundary conditions.

The experimental results for pipe flows /19-24/ included in Fig. 11 scatter widely. This has also been found in the review by Lawn /4/ for the rms-values at a fixed point in the channel. Following the analogy to the behaviour of the eddy conductivity, especially the data by Fuchs /19/ and by Rust & Sesonske /21/ should be higher. And the decrease in the air data by Lawn & White /24/ causes at least some astonishment. It is true, any decreases of the rms maximum values have also been detected at higher, but constant, Prandtl numbers in an overview by the author in /7/.

One reason for the decrease in the experimental high Prandtl number data is the limited spatial resolution capability of the thermal sensors used: The maximum of the rms temperature fluctuation profiles moves in non-normalized coordinates with increasing Prandtl numbers and Reynolds numbers nearer to the walls and looses thereby radial spatial extension. Thus the narrow peak of the temperature fluctuations can be reduced by sensors with insufficient spatial resolution capabilities. This reason holds also for the numerical air data,

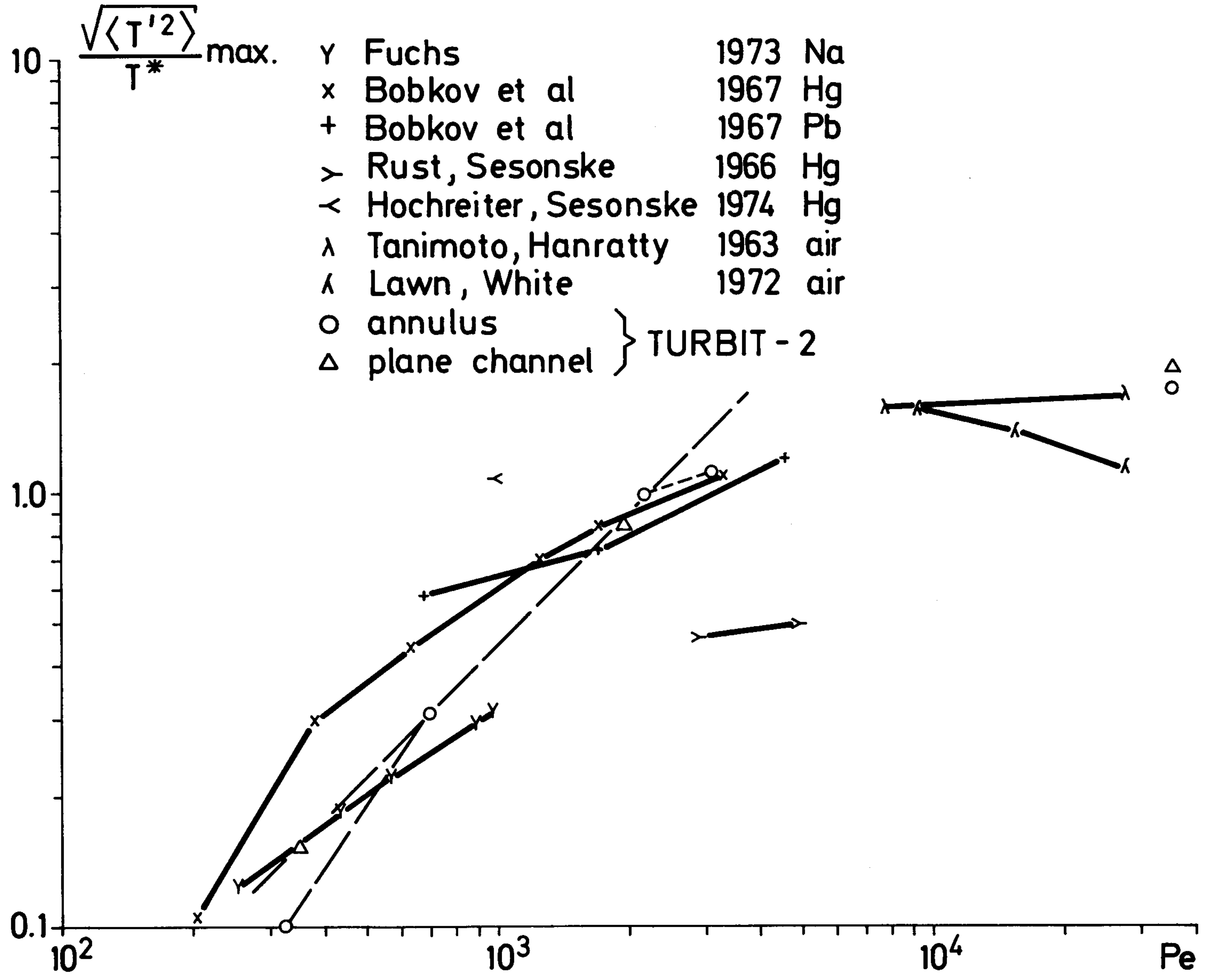

Fig. 11: The influence of Peclet number on the maxima of the radial temperature rms-value profiles. All experimental data by /19 to 24/ are for pipes. The heat flux temperature T^{*} used for normalization of Fuchs' data has been deduced from his figures for T and T^{+}.

but it canot be applied to interpret the wide scatter of the experimental data for small Peclet numbers because there the spatial extension of the peak in the rms temperature profile is very broad (see Figs. 6 and 7).

Another reason for the decrease in the experimental high Prandtl number data is the limited frequency range of the sensors and electronics used: With increasing Reynolds numbers the energy in the high frequency range of the spectra of the temperature fluctuations increases, but will be filtered off by too slow sensors. Even for the Prandtl number of air the corresponding differences are about 10 to 20 % /8/. Obviously, this argumentation can also be applied to the existing liquid sodium experiments: Fuchs /19/, for example, used due to hum and noise disturbancies an electronic with a low pass filter at 10 Hz; Bunschi & Seifritz /25/ used in the same channel and same Peclet number range, and therefore in the same frequency range a faster thermocouple and got considerable temperature fluctuation contributions up to 45 Hz; Bunschi /26/ used again in the same channel a band pass filter at 50 Hz and low pass filter at 100 Hz, and found temperature rms-values 30 % higher than those of Fuchs ; finally, Benkert /27/ shows for a comparable channel and Reynolds number range considerable temperature fluctuations up to 1 kHz.[x] A further open problem is the low frequency cutoff used with all of these experiments. Thus we can only conclude that the data by Fuchs /19/ included in Fig. 11 are surely too low, and that its dependence on the Peclet number is probably not correct.

By the discussion of these uncertainties of experimental temperature fluctuation results it gets evident why Lawn /4/ could not verify his spectral theory to calculate the heat flux correlation coefficient. The corresponding experimental results must scatter widely because they contain the uncertain rms temperature fluctuations by definition. Whereas Lawn cites values for the

---

[x] For Fuchs' measurements a high frequency cutoff of about 600 Hz can be deduced from the recent paper by Genin et al. /28/.

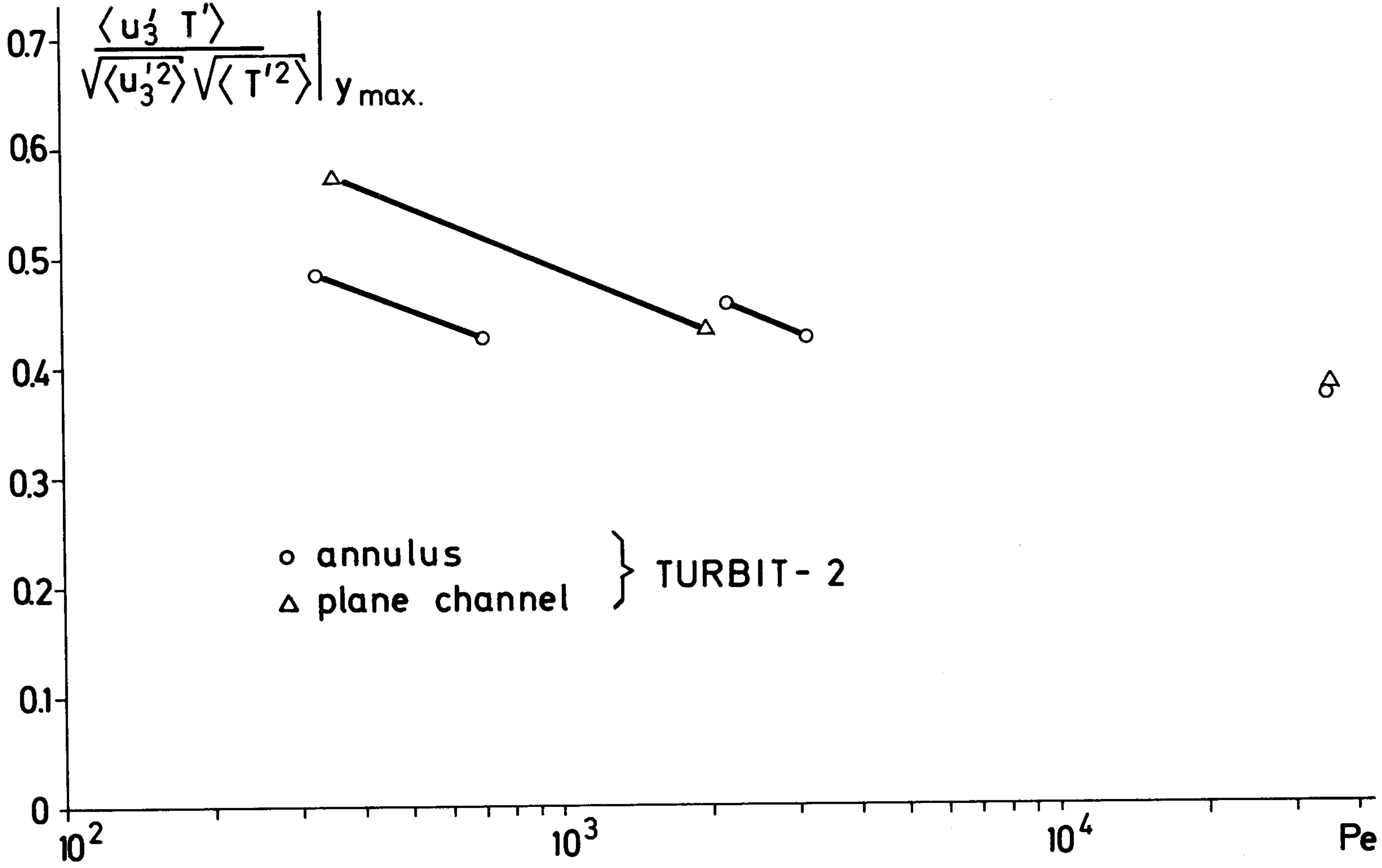

Fig. 12: The dependence of the resolved radial heat flux correlation coefficient on the Peclet number at the position y_{max} of the resolved maximum rms temperature values. The lines connect the numerical results for cases with equal Prandtl numbers and ratios of radii (for identification see Tab. 1).

correlation coefficient (at $y = 0.25$) from 0.15 up to 2.3, the numerical data at the position of the maximum rms temperature values, taken from Figs. 6 and 7 and gathered in Fig. 12, are around 0.45. The numerical results show for each Prandtl number a uniform decrease with increasing Peclet number. The reason for this decrease comes mainly from volume averaging the basic equations (eq. 1) over finite grid volumes: The air data by Hishida & Nagano /11/ show a sharp peak of the heat flux correlation coefficient very near to the wall, near to the outer edge of the conductive sublayer; this maximum is not resolved by the grids used here for air flows. The numerical results given in Figs. 6 and 7 show an increase of the correlation coefficient near the wall when the Peclet number decreases, or when the conductive sublayer grows in thickness. The correlation coefficients react less sensitive on changes in the Peclet number in the inner parts of the channels. Thus, the numerical data confirm the results of Lawn's theory that the heat flux correlation coefficient is, if at all, a weak function of the Peclet number, except for the very low Peclet number cases with $\varepsilon_H/a < 1$ for which the convective turbulent heat flux is insignificant compared to the pure conductive heat flux.

6. Conclusions

The method of direct numerical simulation was applied in this work to calculate turbulent liquid metal flows together with a theory to calculate all coefficients of the subgrid scale models. The numerical results for the temperature fields react very insensitive on changing the theoretically determined coefficients for the subgrid scale heat flux model. The temperature fluctuation fields resulting from the low Peclet number simulations do not depend on any coefficients in the temperature equations; the spatial structures in these fields follow qualitatively the tendencies of the results for larger

Peclet numbers, for which the subgrid scale heat flux model is relevant. The Nusselt numbers in case of plane channel flows, and some temperature and eddy conductivity profiles in case of annular flows agree with published experimental data. From this we conclude that the theory to calculate the subgrid scale coefficients gives adequate results over the total Peclet number range under consideration.

The turbulent heat flux data deduced from the numerical results indicate complex dependence on Reynolds number, Prandtl number, Peclet number, thermal boundary conditions and on the ratio of radii. The large scatter of the empirical correlations for the Nusselt number in annular flows is mainly due to problems in formulating appropriate eddy conductivity profiles accounting for all cited parameters. The deduction of reasonable eddy conductivities or turbulent Prandtl numbers still remains an open problem for all liquid metal flows in annuli and other complicated channels. The numerically deduced eddy conductivity profiles for liquid metal annular flows added in this work are the first directly determined data in the literature. These results can give pointwise support to the development of better models.

Existing statistical data on turbulent temperature fluctuations in liquid metal flows show also large uncertainties. The main reasons in this context are the limited spatial and time resolution capabilities in most experiments. The numerical results for the rms temperature fluctuations are within the range of experimental data; they furtheron show qualitatively comparable functional dependence as the eddy conductivity. The evaluated radial heat flux correlation coefficient is for all cases near to most published data for air flows; it is a very weak function on the Peclet number etc. Thus, these numerical results confirm Lawn's theory.

The method of direct numerical simulation seems to be rather expensive due to its computer storage and computing time requirements; but, compared to experiments with liquid metals it is comparable or even less expensive, and covers less problems. Especially with respect to turbulence model development for very small Peclet numbers it is easier to insure clean conditions by use of a numerical model than by experiments.

7. Literature

/1/ B.A. Kader, A.M. Yaglom
Heat and mass transfer laws for fully turbulent wall flows
Int. J. Heat Mass Transfer 15, 1972, 2329-2351

/2/ A.J. Reynolds
The prediction of turbulent Prandtl and Schmidt numbers
Int. J. Heat Mass Transfer 18, 1975, 1055-1069

/3/ N.V.K. Dutt
Turbulent heat transfer characteristics of liquid metals
J. Scient. Ind. Res. 36, 1977, 165-171

/4/ C.J. Lawn
Turbulent temperature fluctuations in liquid metals
Int. J. Heat Mass Transfer 20, 1977, 1035-1044

/5/ J.W. Deardorff
A numerical study of three-dimensional turbulent channel flow at large Reynolds numbers
J. Fluid Mechanics 41, 1970, 453-480

/6/ U. Schumann
Subgrid scale model for finite difference simulations of turbulent flows in plane channels and annuli
J. Comp. Phys. 18, 1975, 376-404

/7/ G. Grötzbach
Direkte numerische Simulation turbulenter Geschwindigkeits-, Druck- und Temperaturfelder bei Kanalströmungen
Diss., Universität Karlsruhe, Rep. KfK 2426, 1977

/8/ G. Grötzbach, U. Schumann
Direct numerical simulation of turbulent velocity-, pressure- and temperature-fields in channel flows
Symp. on turbulent shear flows, Penn. St. Univ., April 18-20, 1977, Proc. Turbulent Shear Flows I, Ed. F. Durst et al., Springer 1979, 370-385

/9/ G. Grötzbach
Numerical investigation of the influence of secondary
flows on characteristic turbulence data
KfK 2553, 1978

/10/ J.O. Hinze
Turbulence
Mc Graw Hill, New York, 1975, 2nd edition

/11/ M. Hishida, Y. Nagano
Structure of turbulent velocity and temperature fluctuations
in fully developed pipe flow
Trans. ASME C, J. Heat Transfer 101, 1979, 15-22

/12/ O.E. Dwyer, P.J. Hlavac, B.G. Nimmo
Eddy diffusivity of heat transfer in the radial direction
for turbulent flow of mercury in annuli
Int. J. Heat Mass Transfer 20, 1977, 141-151

/13/ G. Grötzbach
Direct numerical simulation of laminar and turbulent
Bénard convection
to be published

/14/ H. Gräber
Der Wärmeübergang in glatten Rohren, zwischen parallelen
Platten, in Ringspalten und Längs-Rohrbündeln bei exponentieller Wärmeflußverteilung in erzwungener laminarer oder
turbulenter Strömung
Int. J. Heat Mass Transfer 13, 1970, 1645-1703

/15/ O.E. Dwyer
Heat transfer to liquid metals flowing turbulently between
parallel plates
Nucl. Science and Engng, 21, 1965, 79-89

/16/ W.M. Kays, E.Y. Leung
Heat transfer in annular passages - hydrodynamically developed
turbulent flow with arbitrarily prescribed heat flux
Int. J. Heat Mass Transfer 6, 1963, 537-557

/17/ O.E. Dwyer
On the transfer of heat to fluids flowing through pipes, annuli, and parallel plates
Nucl. Science and Engng, 17, 1963, 336-344

/18/ H. Barthels
Darstellung des Wärmeüberganges in konzentrischen Ringspalten unter Benutzung der Analogie zwischen Impuls- und Wärmeaustausch
Dissertation, Technische Hochschule Aachen, Rep. Jül-506-RB, 1967

/19/ H. Fuchs
Wärmeübergang an strömendes Natrium - Theoretische und experimentelle Untersuchungen über Temperaturprofile und turbulente Temperaturschwankungen bei Rohrgeometrie
Diss., Eidgen. Technische Hochschule Zürich, EIR-Bericht Nr. 241, Würenlingen 1973

/20/ V.P. Bobkov, M.Kh. Ibragimov, V.I. Subbotin
Statistische Daten über turbulente Temperaturschwankungen in der Strömung
Zhidkie metally, Moskau 1976, 53-71, german translation KfK-tr-372

/21/ J.H. Rust, A. Sesonske
Turbulent temperature fluctuations in mercury and ethylene glycol in pipe flow
Int. J. Heat Mass Transfer 9, 1966, 215-227

/22/ L.E. Hochreiter, A. Sesonske
Turbulent structure of isothermal and nonisothermal liquid metal pipe flow
Int. J. Heat Mass Transfer 17, 1974, 113-123

/23/ S. Tanimoto, T.J. Hanratty
Fluid temperature fluctuations accompanying turbulent heat transfer in a pipe
Chem. Engng. Sci. 18, 1963, 307-311

/24/ C.J. Lawn, R.S. White
The turbulence structure of heated pipe flow
CEGB Report RD/B/N 2159, 1972

/25/ H. Bunschi, W. Seifritz
A fast-response thermocouple for temperature fluctuation measurements in sodium coolants
Nucl. Technol. 27, 1975, 523-525

/26/ J. Bunschi
Turbulente Temperaturschwankungen im flüssigen Natrium
Diss., Eidgen. Technische Hochschule Zürich, Rep. AF-NST-13, Würenlingen, 1977

/27/ J. Benkert
Untersuchungen von Temperaturfluktuationen in flüssigem Natrium zur Ermittlung charakteristischer Strömungsparameter und Thermoelementübertragungsfunktionen
Diss., Technische Universität Hannover, 1977

/28/ L.G. Genin, E.V. Kudryavtseva, Yu.A. Pakhotin, V.G. Sviridov
Structure of the temperature field associated with turbulent flow in pipes
High Temperature 17, 1979, 445-451

8. Appendix: TURBIT-2 - Plotoutput for an annular flow of sodium with Pe = 700.

To complete the numerical results given in chapter 4 a profile - plotoutput of the analyzing part of the TURBIT-2- program is included here for the annular flow of sodium with Pe = 700. The case specifications are given in Tab. 1 and 2 (p.15). From Tab. 3 (p.17) follows that no subgrid scale heat flux model is used.

The numerical results given in Tab. 4 and in the following computer plots are averaged over the time dependent three-dimensional results for 43 different time steps within a time interval of $\Delta t_{av} = 1.25$ at the end of the simulation. Typical relative standard deviations tsd for this case are 3 to 10 % (see Fig. 7, p. 25).

The nomenclature used is as given on page V. Application of the averaging operator $\overline{Y}^j$ has not been indicated on the figures; this operator has been used in all cases in which data have been correlated not defined on the same place in the staggered grid. The following symbols have been introduced in addition:

A_{ij}	constants in the Rotta-pressure strain model (i,j = 1,2,3), for Ref. see /7/ $\langle p' (\frac{\partial u'_i}{\partial x_j} + \frac{\partial u'_j}{\partial x_i})\rangle = - A_{ij} \frac{\varepsilon}{E_{tot}} (\langle u'_i u'_j\rangle - \frac{2}{3}\delta_{ij} E_{tot})$
B	constant in the proposal by Fulachier, Dumas /A3/ $B = \left(\frac{2\langle E_{tot}\rangle}{\sqrt{\langle {}^{v}\overline{T}'^{2}\rangle}}\right)^{1/2} \left\lvert \frac{\delta_3 \langle {}^{v}\overline{T}\rangle}{\delta_3 \langle {}^{1}\overline{u}_1\rangle} \right\rvert$
C_{iT}	constant in the Launder-pressure scrambling model, for Ref. see /7/ $\langle p' \frac{\partial T'}{\partial x_j}\rangle = - C_{1T}\frac{\varepsilon}{E_{tot}}\langle u'_j T'\rangle + C_{2T}\langle u'_i T'\rangle \frac{\partial\langle u_j\rangle}{\partial x_i}$
E_{ii}	energy spectra, calculated from the space-dependent data
E_{tot}	total turbulence energy $E_{tot}(\underline{x}) = ({}^{i}\overline{u}'_i(\underline{x}))^2/2 + {}^{v}\overline{E'}(\underline{x})$
K_1	one-dimensional wave number
$L_{ij,k}$	correlation length of $R_{ij}(\underline{x}_k)$ in the $\underline{x}_k$-direction $= \frac{2}{X_k}\int_0^{X_{k/2}} R_{ij}(\underline{x}_k)\, d\underline{x}_k$
Pr_{tB}	turbulent Prandtl number recalculated from B /A3/ $Pr_{tB} = \left\lvert \frac{\langle {}^{1}\overline{u}'_1 {}^{3}\overline{u}'_3\rangle + \langle {}^{3}\overline{u'_1 u'_3}\rangle}{\langle {}^{3}\overline{u}'_3 {}^{v}\overline{T}'\rangle} \right\rvert \left(\frac{\sqrt{\langle {}^{v}\overline{T}'^{2}\rangle}}{2\langle E_{tot}\rangle}\right)^{1/2} B$
$R_{ij}(\underline{x}_k)$	two-point correlation $= \frac{\langle u'_i(\underline{x}) u'_j(\underline{x}+\underline{x}_k)\rangle}{\langle u'_i(\underline{x}) u'_j(\underline{x})\rangle}$

(VZ,VP,VR)	velocity vector $= (u_1, u_2, u_3) = (u, v, w) = \underline{u}$
$\underline{x}_j$	translation vector $= (x_1, 0, 0) \quad j = 1$ $= (0, x_2, 0) \quad j = 2$ $= (0, 0, x_3) \quad j = 3$
$v_{\overline{Y'}}$, $j_{\overline{Y'}}$	subgrid scale value for any quantity Y

The radial velocity profiles (Fig. 1-3) follow the logarithmic law indicated. The numerical data tend to larger values near the maximum of the outer wall profile and to smaller values in the inner wall profiles. This is also observed in experimental data /A1/. The radial distribution of the turbulent pressure fluctuations is comparable to that in other annular flows /7, p.99/.

The negative values of the averaged radial temperature profile given in Fig. 5 are due to a Galilean transformation to maximize the permissible time step width. In the semilogarithmic presentation the temperature profile largely follows the Kirillov law /19/:

$$\begin{aligned} T^+ &= Y^+ \, Pr && (Y^+ \, Pr < 1) \\ T^+ &= 4.31 \log(Y^+Pr+1)+0.065Y^+Pr-0.36 && (1 < Y^+Pr < 11.7) \\ T^+ &= 5.75 \log (Y^+Pr) - 1 && (11.7 < Y^+Pr) \end{aligned}$$

To the directly evaluated rms-values of the large scale velocity fluctuations (Fig. 8) and to the turbulence energy (Fig. 22) a subgrid scale part has been added resulting from the subgrid scale kinetic energy equation.
The rms-values of pressure fluctuations (Fig. 9) and temperature fluctuations (Fig. 10) contain no subgrid scale parts.

Two-point correlations calculated at the center of the channel and the corresponding correlation lengths are shown in Fig. 11 to 13 for the three velocity components. Similarly, several auto-and cross-correlations for the resolved fluctuations of temperature, pressure and turbulence energy are shown in Fig. 14 to 17. Especially from R_{TT} may be concluded that a larger periodicity length X_1 would be more appropriate. The X_1 value chosen is more appropriate for larger Peclet numbers /7, Fig. 37/).

The skewness of the velocity and temperature fluctuations show considerable scatter (Fig. 18-19). Nevertheless, the skewness-profile for u'_3 is typical for all calculated annular flows. The flatness indicates nearly Gaussian distribution of velocity and temperature fluctuations (Fig. 20-21).

Fig. 22 to 24 show evaluations of the additional transport equation for the subgrid scale energy ${}^{V}\overline{E'}$. The total subgrid scale energy dissipation ${}^{V}\overline{\varepsilon'}_{tot}$ is described in terms of a Rotta-type model /7,8/. In this model the low Reynolds number part (no. II) is important near the walls.

Evaluations for the total turbulence energy equation are given in Fig. 25 to 28. The dissipation is mostly contained in the unresolved subgrid scale structure. Subgrid scale parts for the turbulent diffusion (TUDI, Fig. 27 and 35) have to be neglected with the present model.

The evaluated pressure strain correlations (Fig. 29) appearing in the turbulent shear stress equations have been used to calculate the coefficients A_{ij} (Fig. 30) of the Rotta model (see nomenclature on p. 43). The values agree qualitatively with the sequence found for plane channel flows /A2/: $A_{33} < A_{11} < A_{22}$. The pressure scrambling correlations (Fig. 31) appearing in the turbulent heat flux equations have been used to calculate the coefficients C_{iT} (Fig. 32) of the Launder model (see nomenclature on p. 43). As for higher Prandtl numbers /7/ the coefficient C_{1T} is constant only in regions where the temperature field is nearly homogeneous.

The radial turbulent shear stress is dominated by the directly resolved part (Fig. 33). The radial turbulent heat flux evaluated needs not to be completed by a subgrid scale part because the subgrid scale heat flux model is zero (Fig. 34). The radial profile of the pressure-temperature cross correlation (Fig. 36) is comparable to that for higher Prandtl numbers. In /7, p. 101/ it is discussed that this term which cannot be determined experimentally is not appropriately accounted for in some existing statistical turbulence models.

The cross correlation coefficients given in Fig. 37 and 38 show nearly horizontal distributions in the inner and outer zone of the channel. A comparable behaviour can not be found with the pressure-temperature cross-correlation coefficient (Fig. 39).

The profiles of the radial eddy diffusivities for momentum and heat are shown in Fig. 40. The scatter of ε_m leads to a widely scattering turbulent Prandtl number (Fig. 41). The proposal of /A3/ to replace the assumption Pr_t = constant by B = constant (see nomenclature, p. 43) for turbulent boundary layers has been tested in Fig. 42 for the annular flow under consideration. As can be seen B is not constant, and the turbulent Prandtl number recalculated from the profile of B is not in agreement with the directly calculated profile. (One possible reason for this disagreement may be that each term appearing in B and Pr_{tB} itself has been time averaged independently from each other).

In the following figures energy spectra are given, which are calculated for several distances from wall 1 from the space-dependent results. The spectra for the velocity components $^1\overline{u}'_1$ to $^3\overline{u}'_3$ (Fig. 43 to 47) show the well known behaviour: At low wave numbers K_1 most of the energy is associated with u_1, and at high wave numbers with u_2. An inertial subrange ($E_{ii} \sim K_1^{-5/3}$) can be identified nearly at each wall distance and for each component, but not within the same wave number range. Therefore, none of the spectra of E_{tot} (Fig. 48 to 52) shows an inertial subrange. As found experimentally /A4/ the Reynolds number is too small to get local isotropy in the high wave number range of the directly resolved velocities. The spectra of the pressure fluctuations partly show an inertial subrange ($E_{pp} \sim K_1^{-7/3}$ /A5/, Fig. 53 to 59) in the inner zone of the channel.

The spectra of the temperature fluctuations (Fig. 60 to 64) show in the total channel an inertial convective subrange ($E_{TT} \sim K_1^{-5/3}$). In addition an inertial diffusive subrange ($E_{TT} \sim K_1^{-3}$ /A6/) is indicated near the center of the channel. All the spectra decrease monotonically with increasing wave numbers, even in the high wave number range. Experience with direct numerical simulation shows that this result is the most important evidence which let us conclude that indeed no subgrid scale heat flux model is necessary for this simulation.

Literature

/A1/ K. Rehme
Turbulente Strömung in konzentrischen Ringspalten
Habilitationsschrift, Universität Karlsruhe, Report KfK 2099, 1975

/A2/ U. Schumann, G. Grötzbach, L. Kleiser
Direct numerical simulation of turbulence
In: Prediction Methods for Turbulent Flows, Ed. W. Kollmann, Hemisphere 1980, 123-258

/A3/ L. Fulachier, R. Dumas
Spectral analogy between temperature and velocity fluctuations in a turbulent boundary layer
J. Fluid Mech. 77, 1976, 257-277

/A4/ G. Lörcher
Laser-Doppler-Messungen von Energiedichtespektren in turbulenter Kanalströmung.
Diss. Universität Karlsruhe, Report KfK 2448, 1977

/A5/ A.S. Monin, A.M. Yaglom
Statistical fluid mechanics: Mechanics of turbulence, Vol. 2
MIT-Press 1975, S. 376 u. S. 516

/A6/ C.H. Gibson
Fine structure of scalar fields mixed by turbulence
Physics of Fluids 11, 1968, 2305-2327

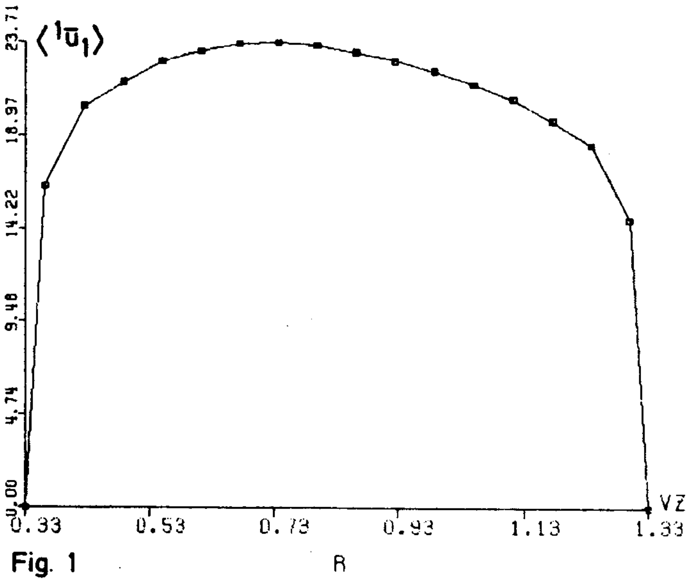

Fig. 1

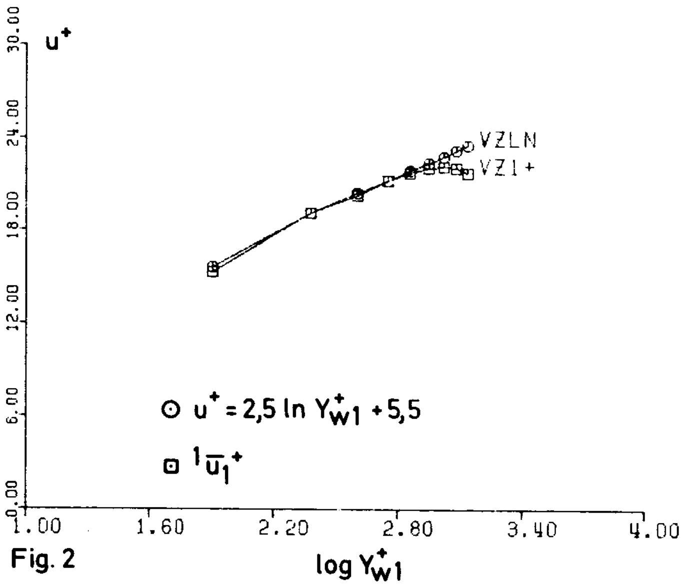

Fig. 2

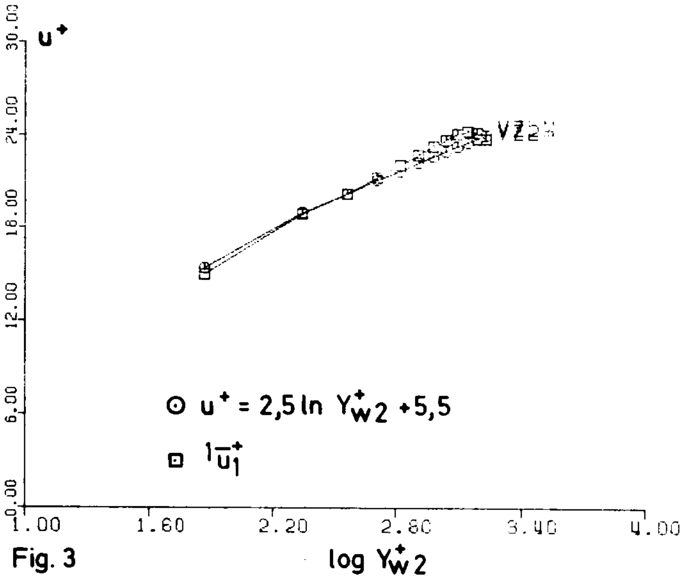

Fig. 3

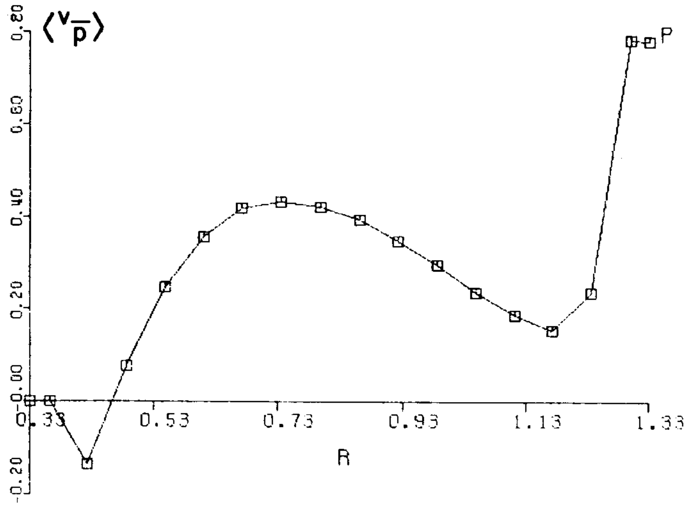

Fig. 4

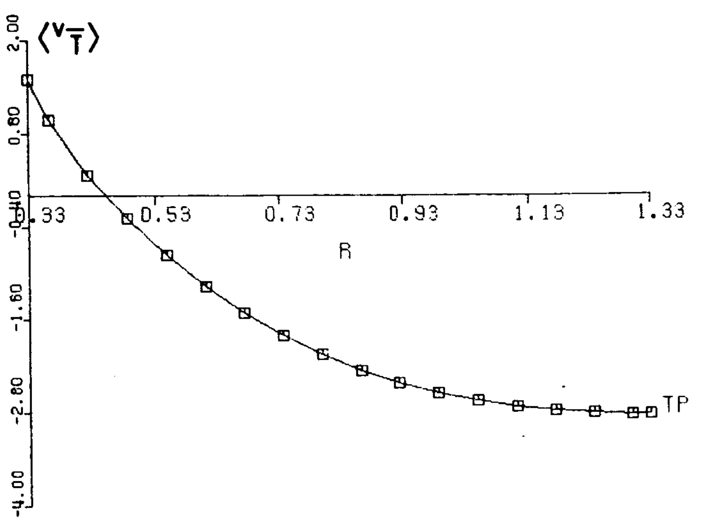

Fig. 5

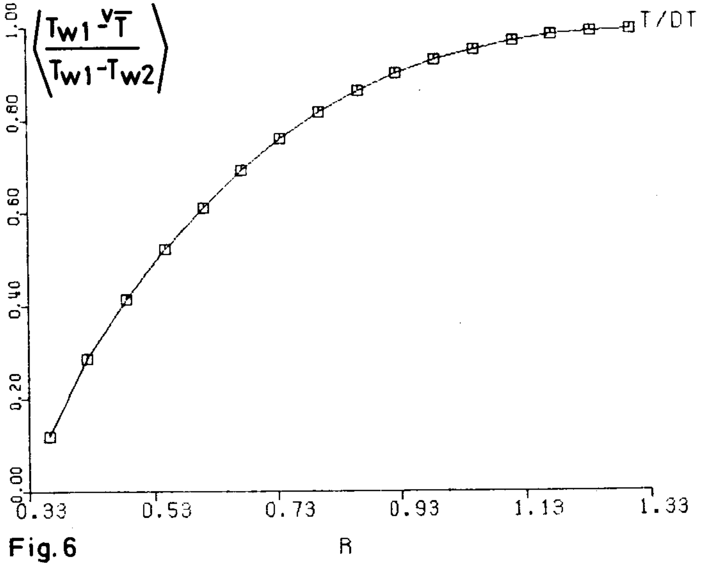

Fig. 6

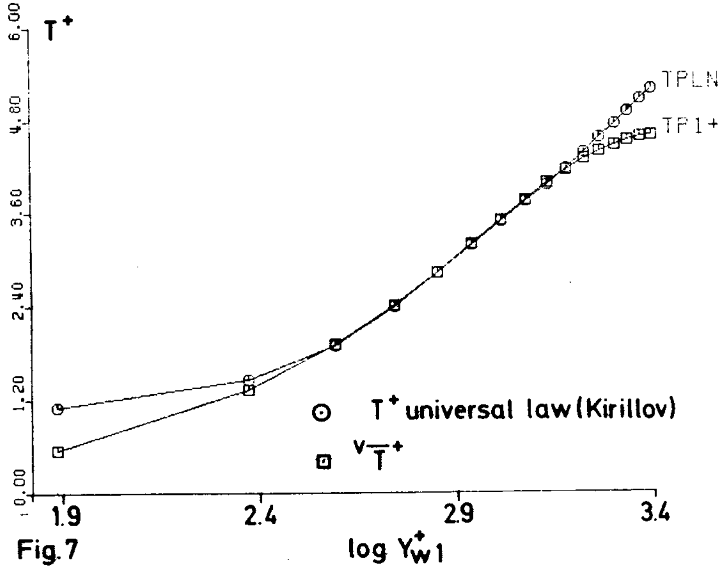

Fig. 7

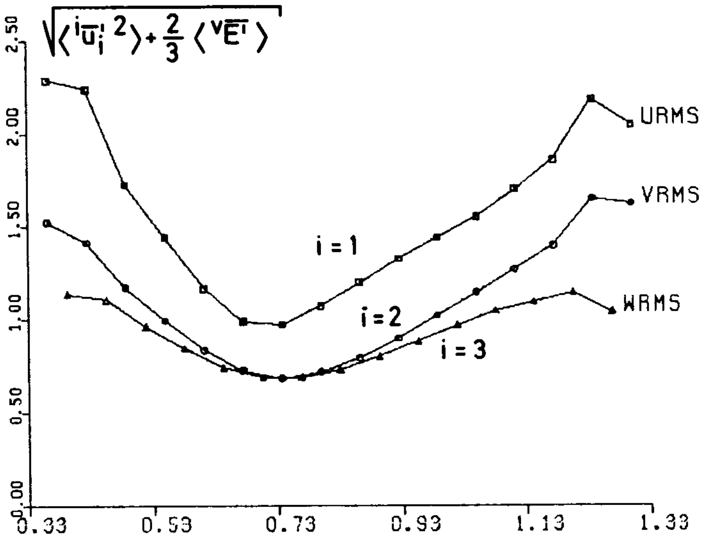

Fig.8

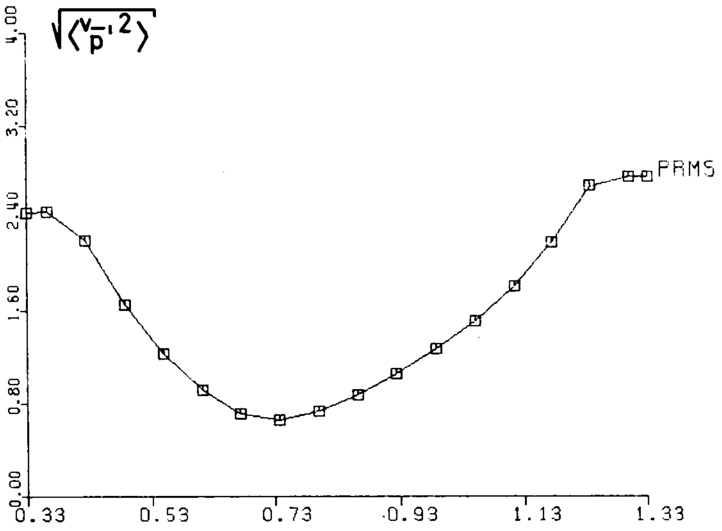

Fig. 9

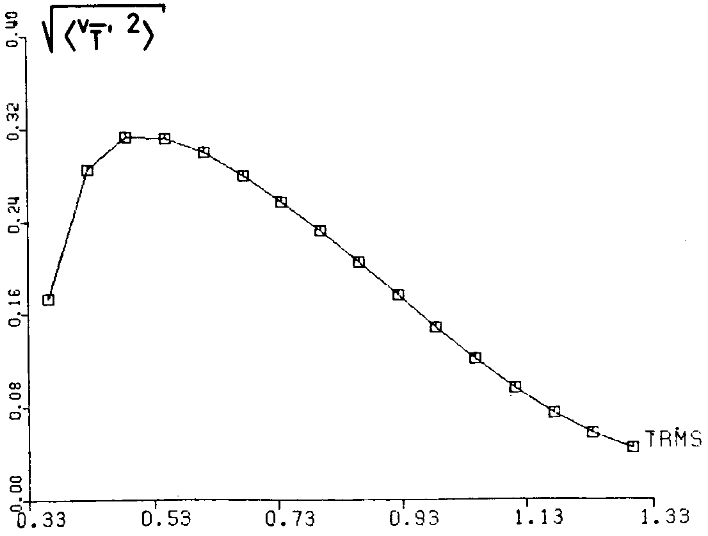

Fig. 10

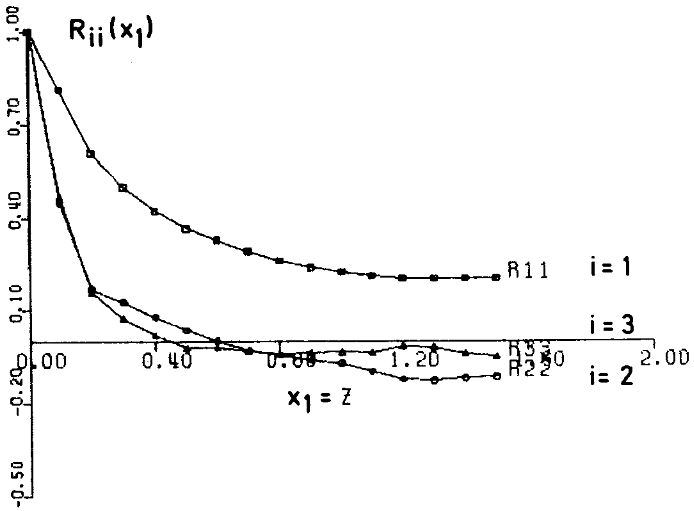

Fig.11

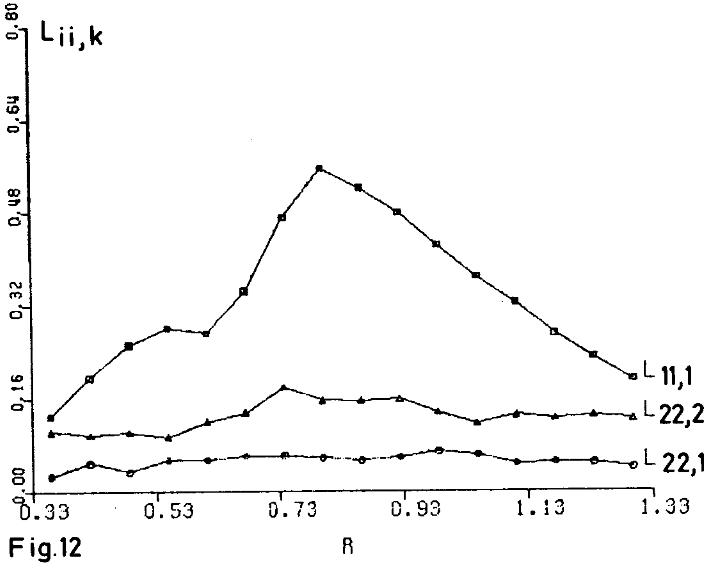

Fig.12

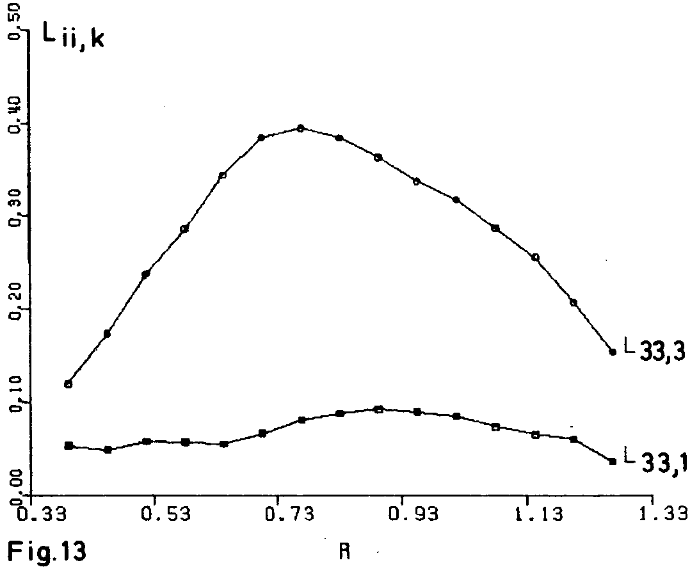

Fig.13

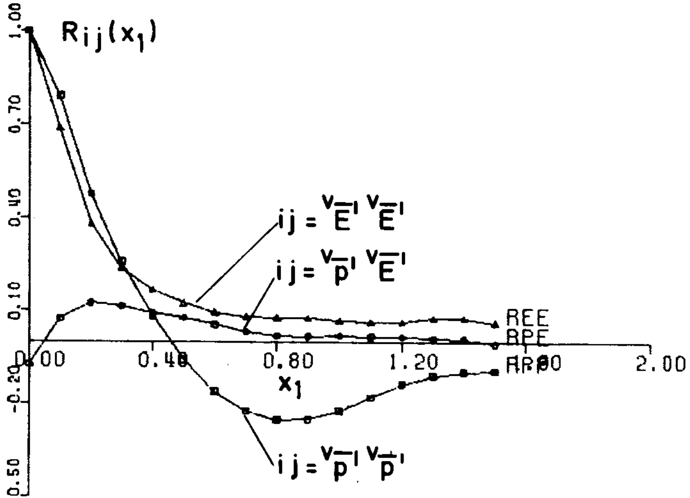

Fig. 14

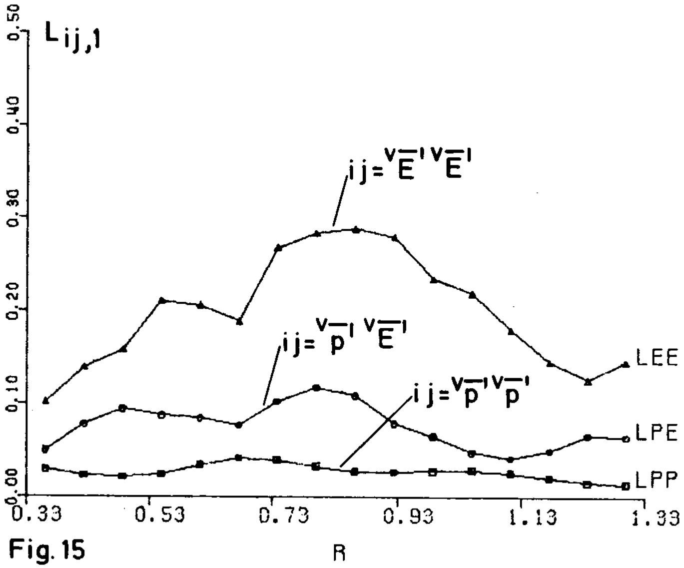

Fig. 15

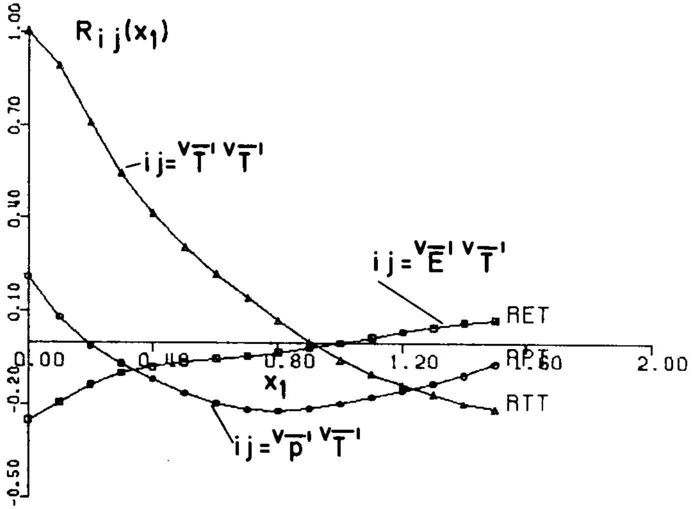

Fig. 16

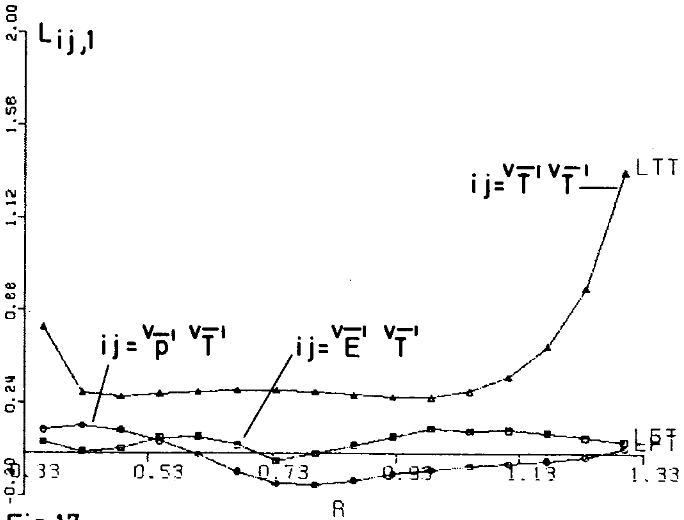

Fig. 17

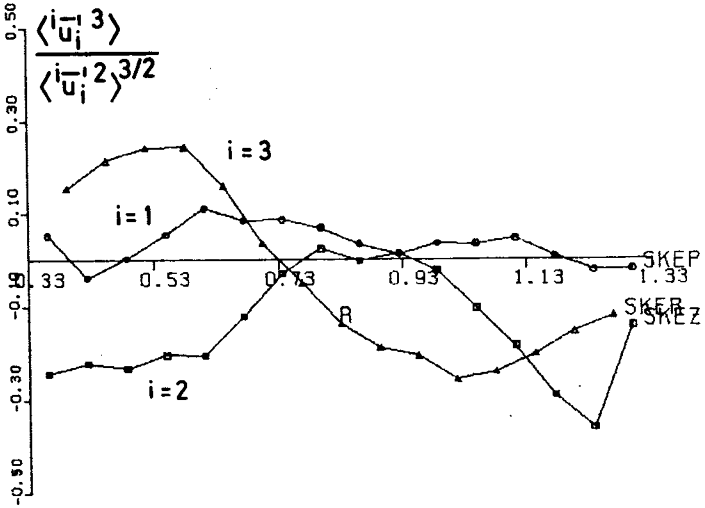

Fig. 18

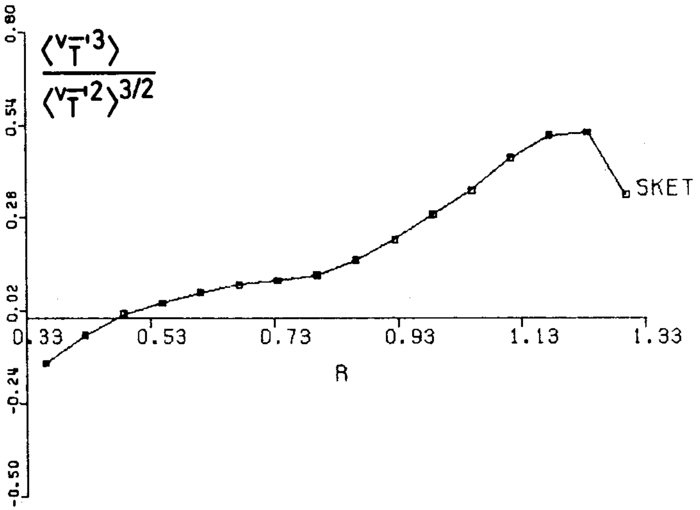

Fig. 19

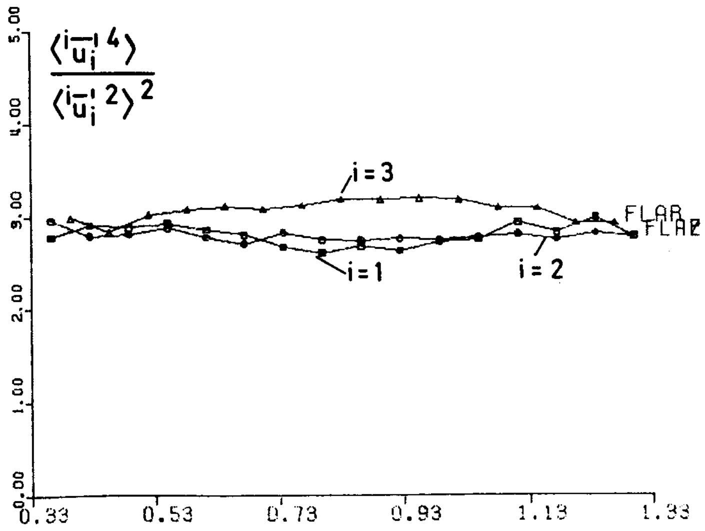

Fig. 20

R

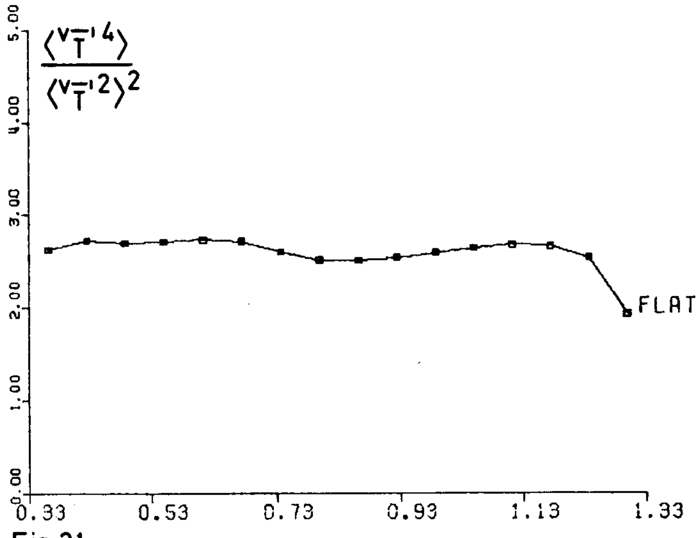

Fig. 21

R

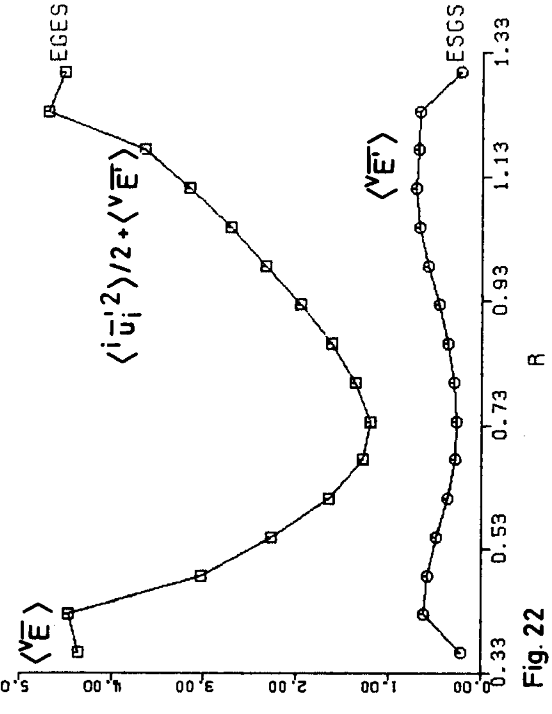

Fig. 22

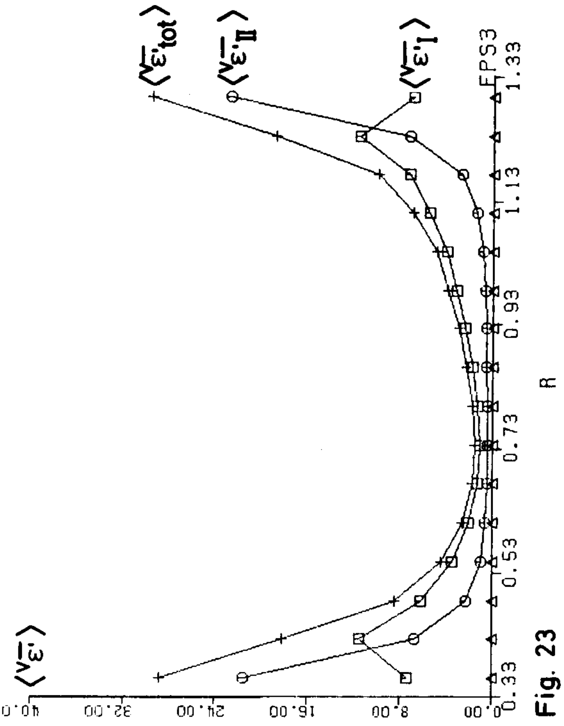

Fig. 23

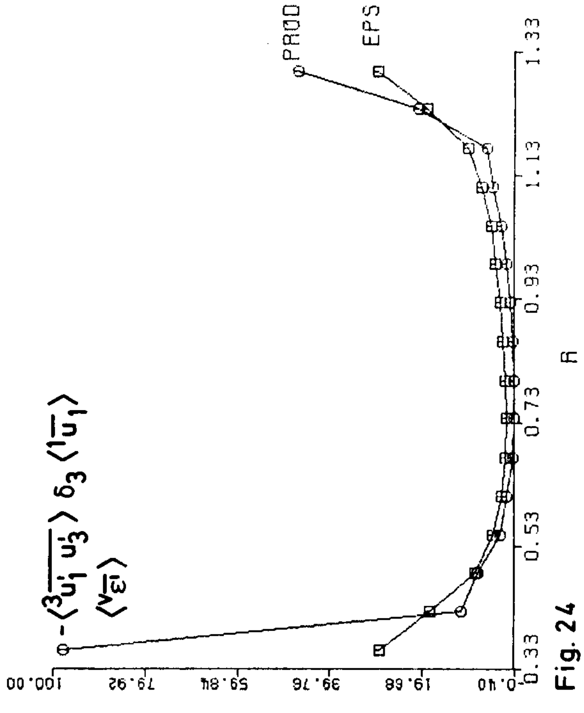

Fig. 24

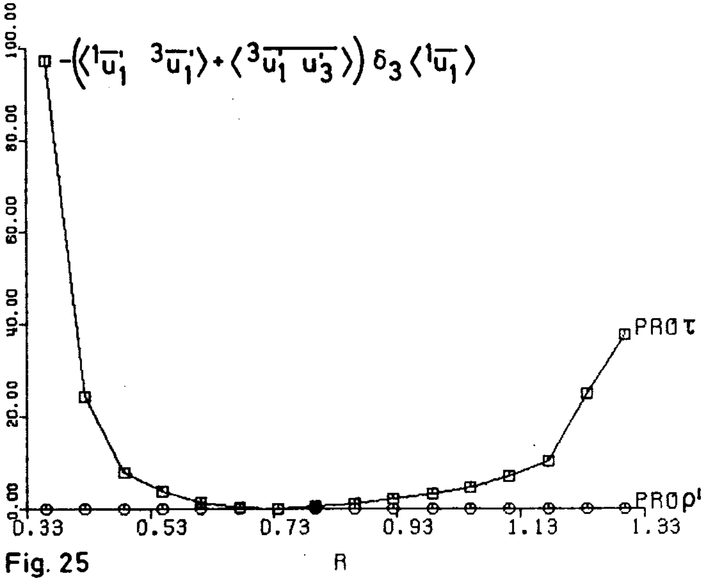

Fig. 25

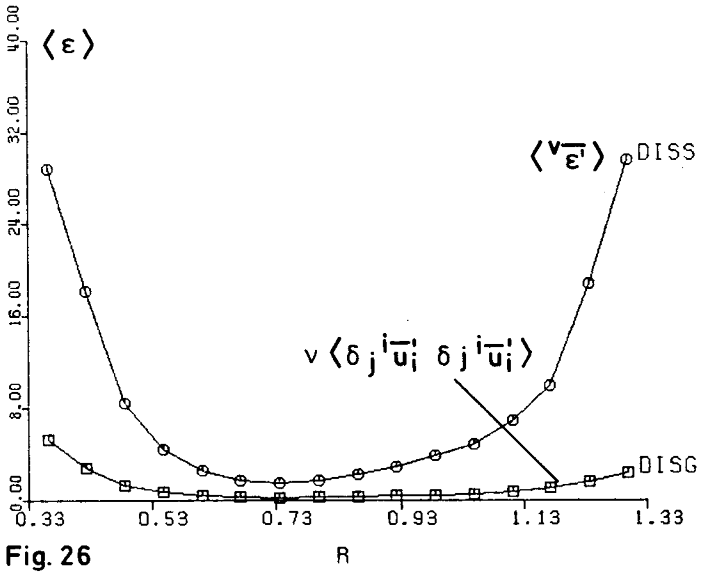

Fig. 26

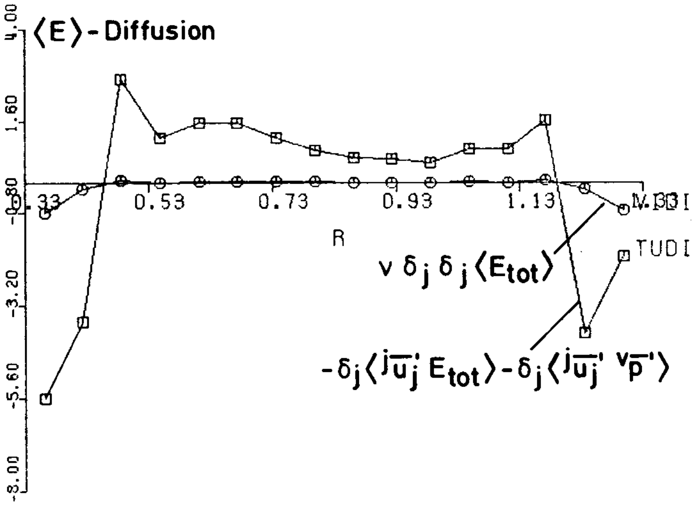

Fig. 27

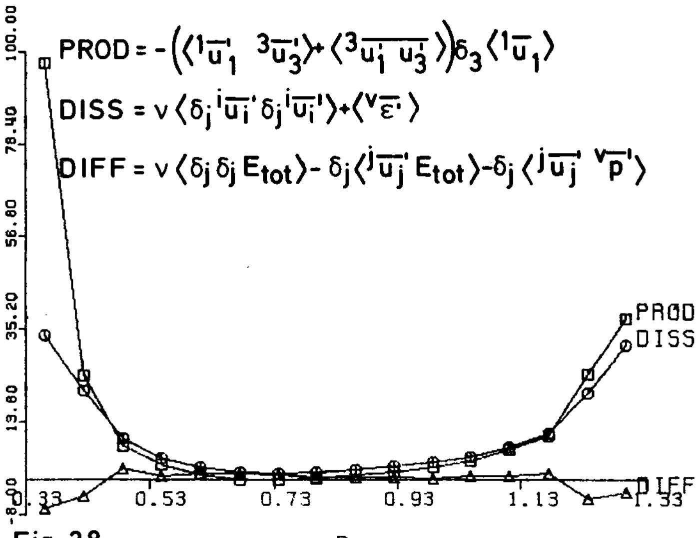

Fig. 28

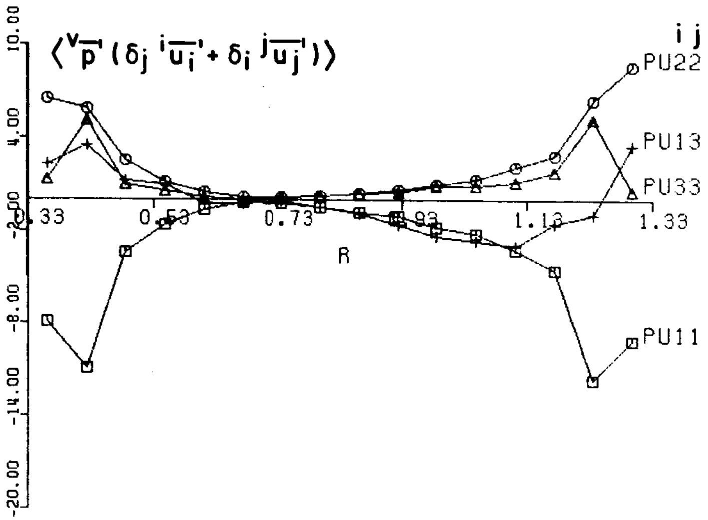

Fig. 29

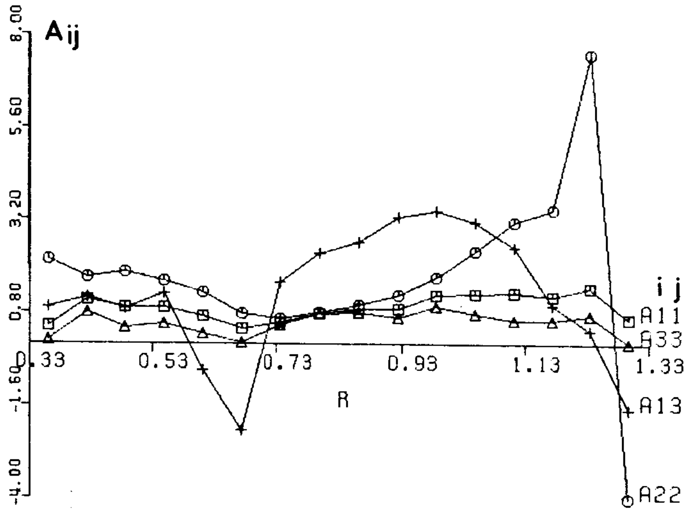

Fig. 30

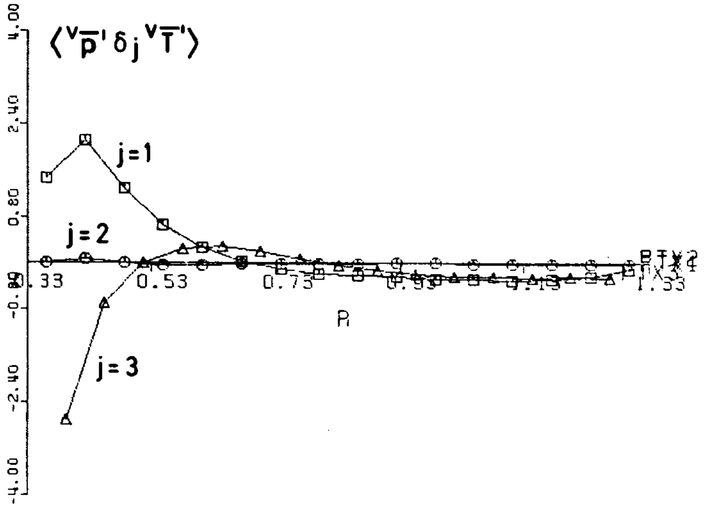

Fig. 31

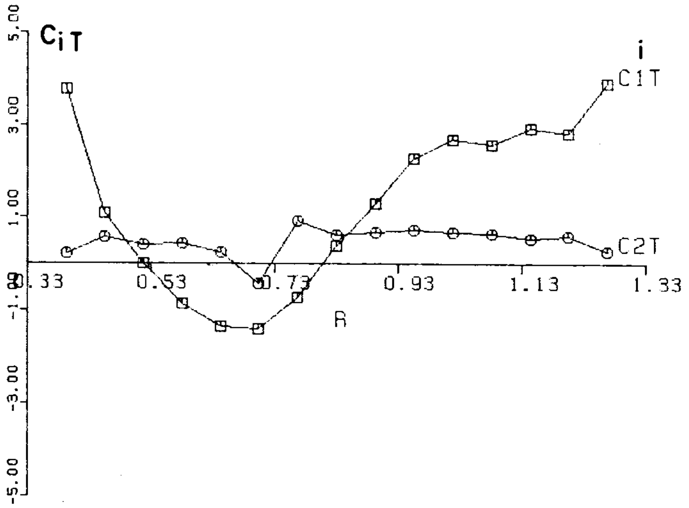

Fig. 32

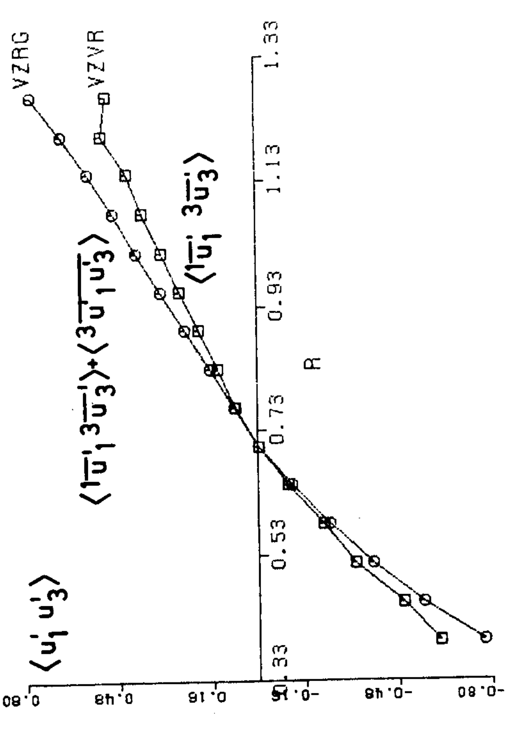

Fig. 33

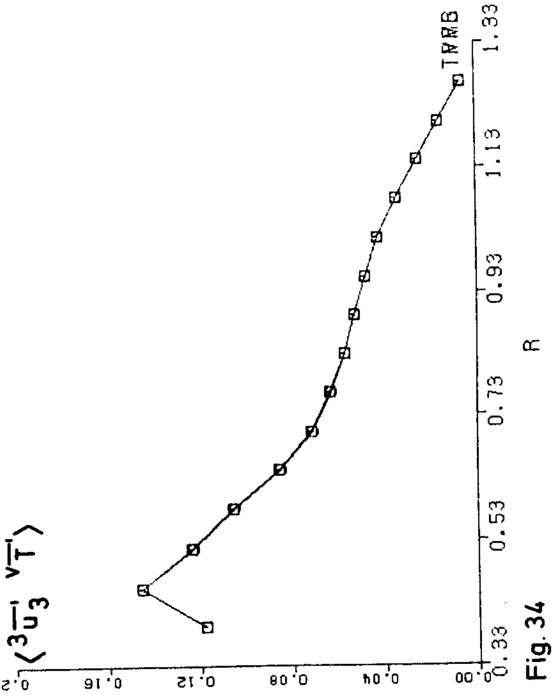

Fig. 34

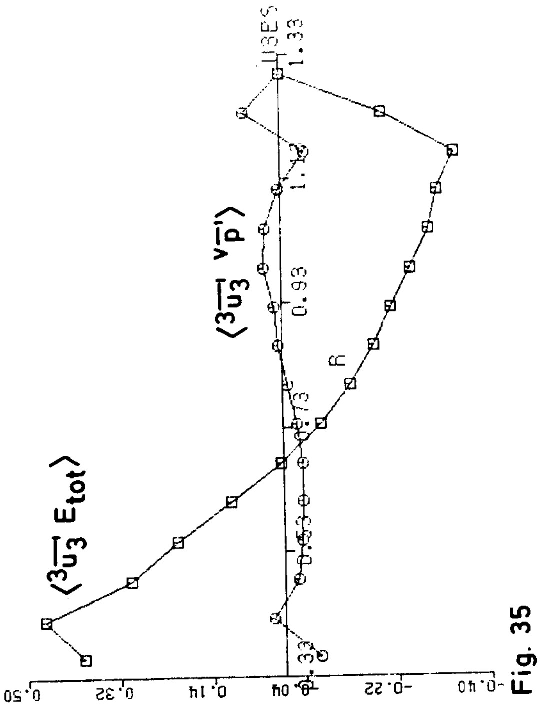

Fig. 35

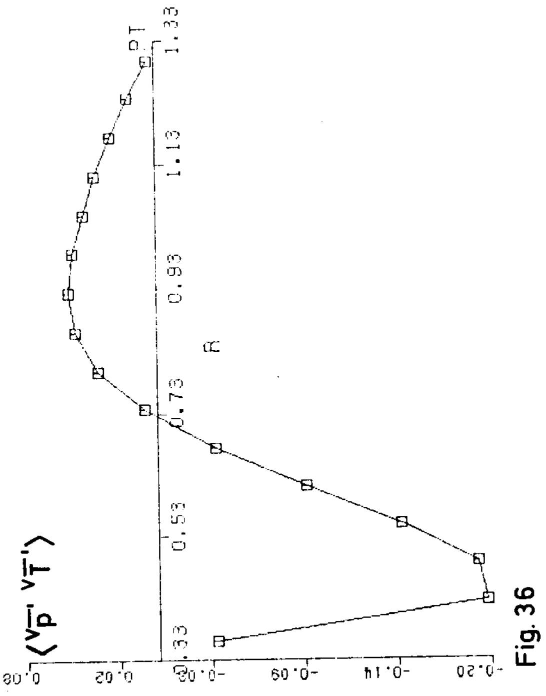

Fig. 36

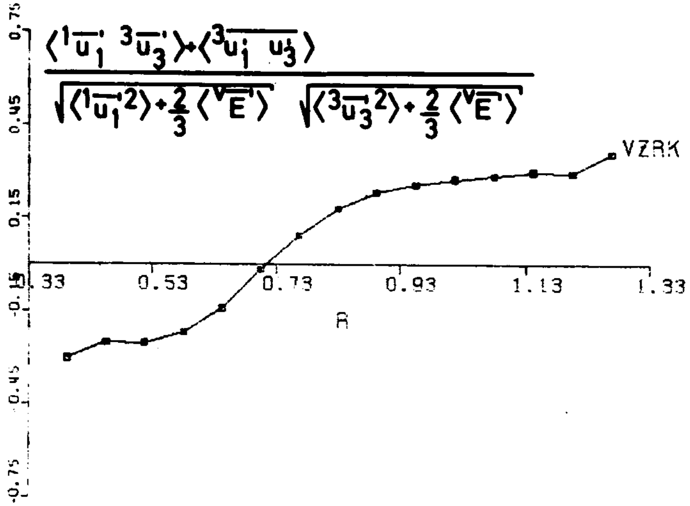

Fig. 37

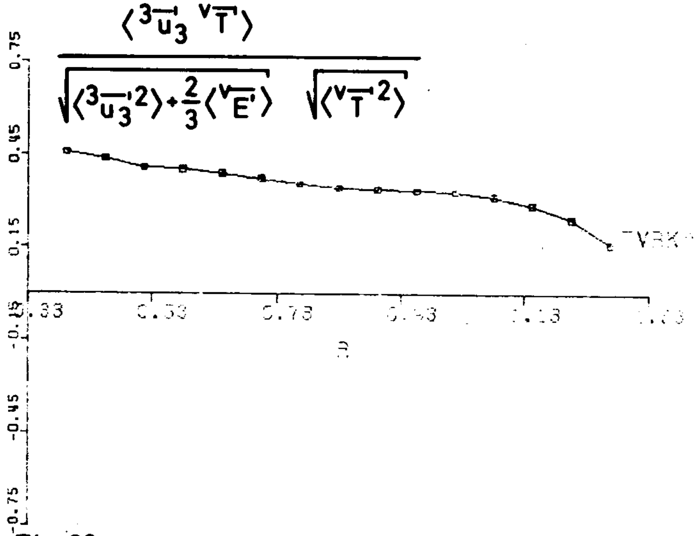

Fig. 38

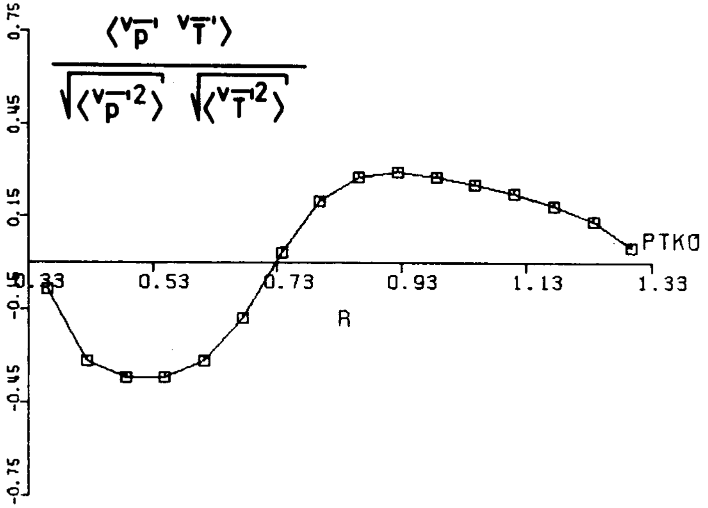

Fig. 39

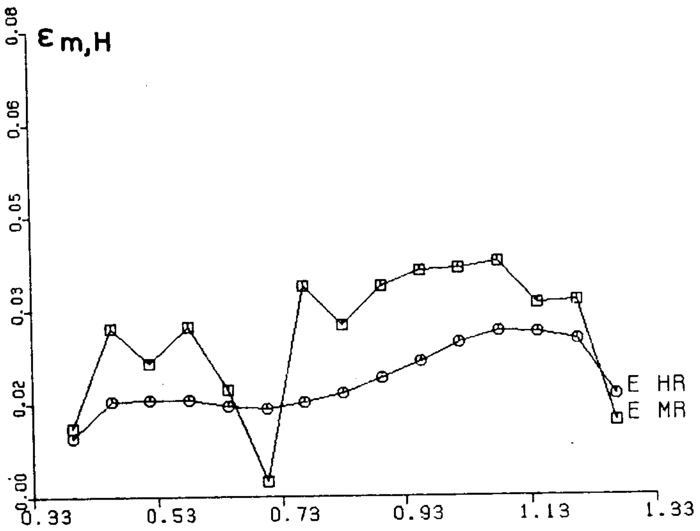

Fig. 40

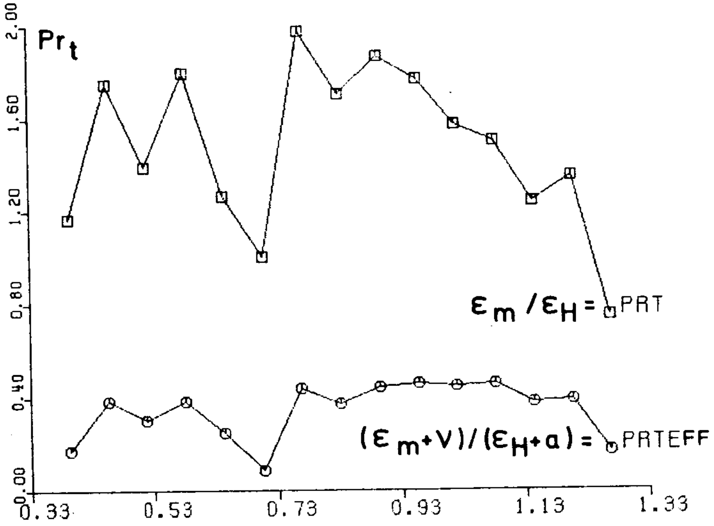

Fig. 41

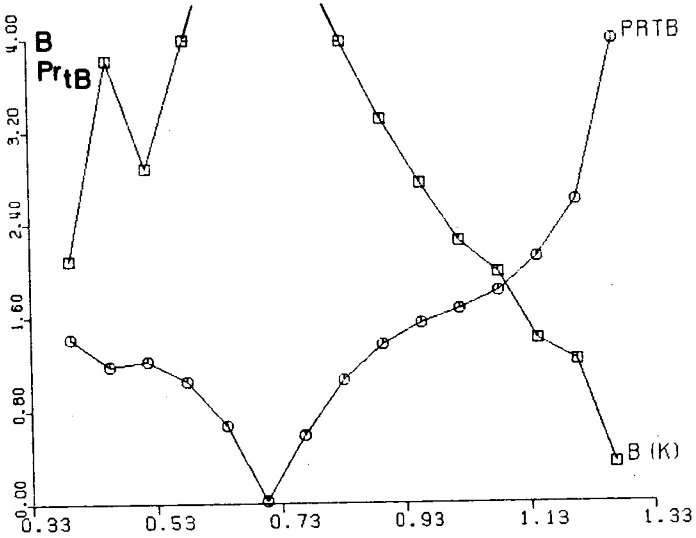

Fig. 42

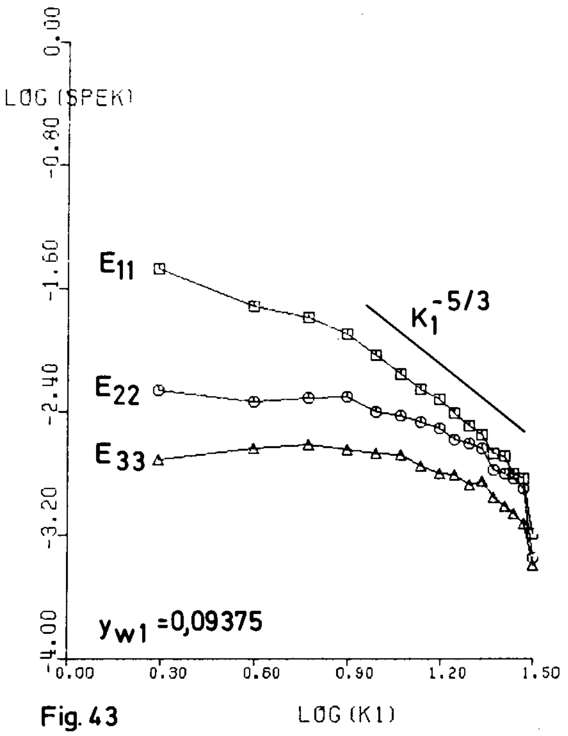

Fig. 43

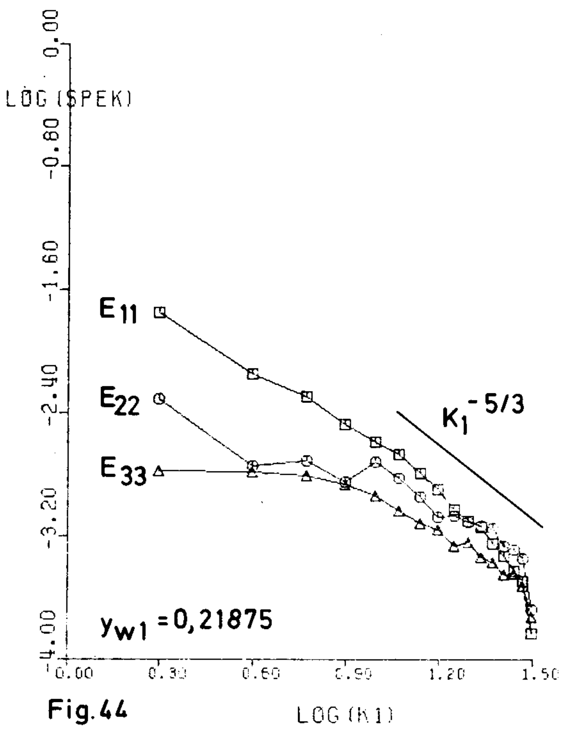

Fig. 44

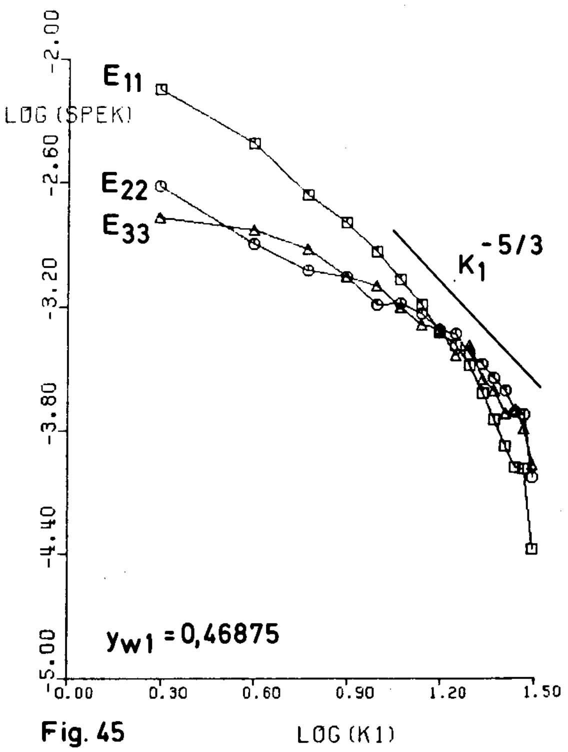

Fig. 45

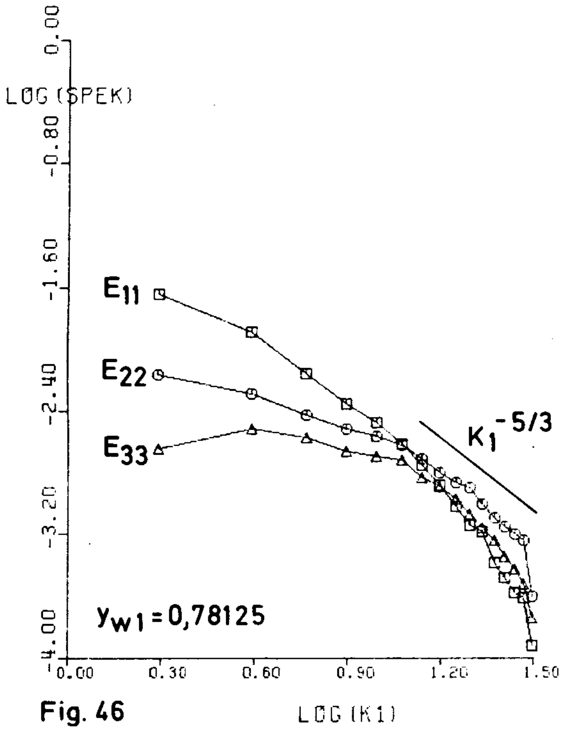

Fig. 46

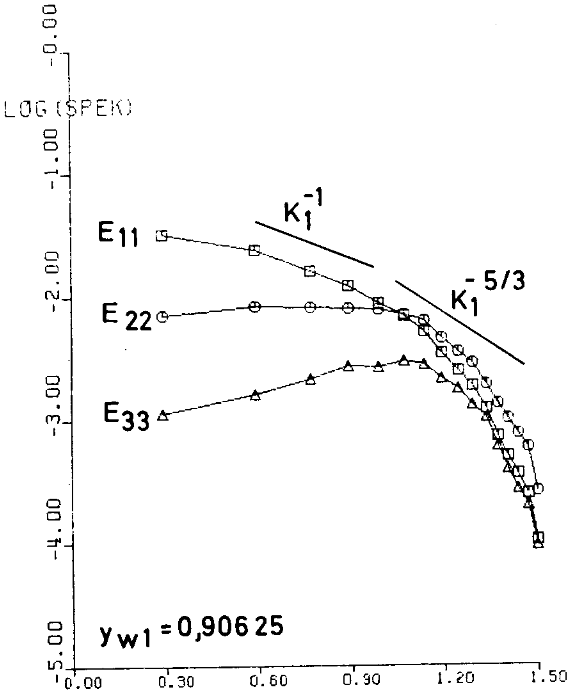

Fig. 47

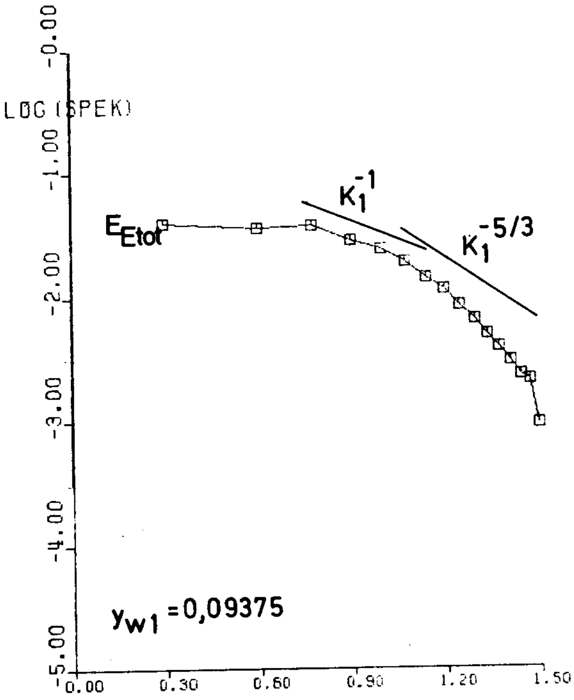

Fig. 48

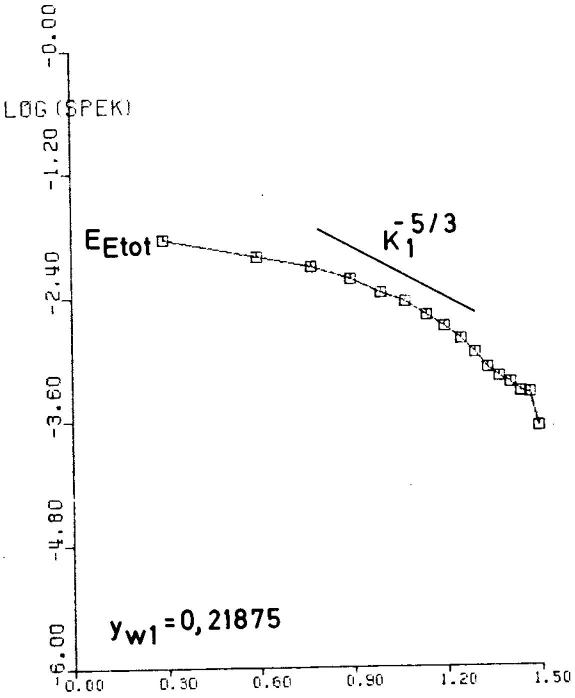

Fig. 49

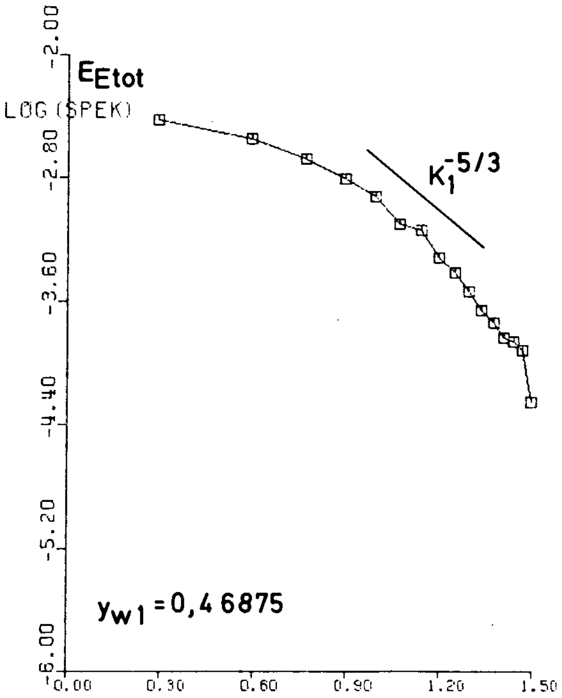

Fig. 50

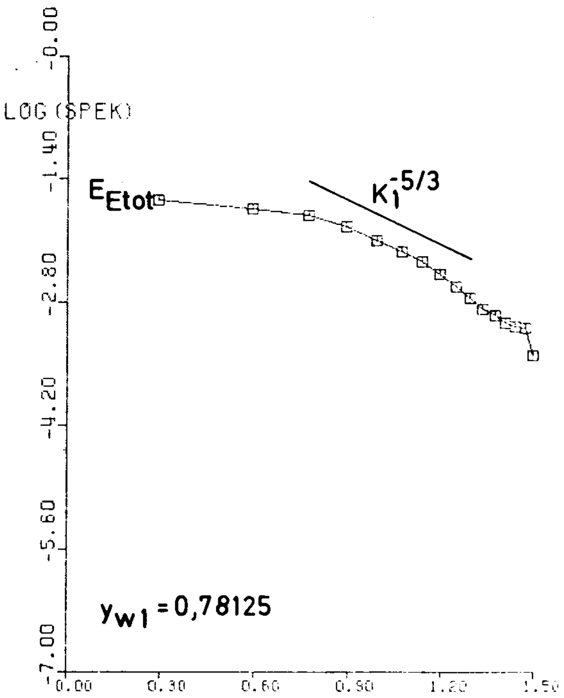

Fig. 51

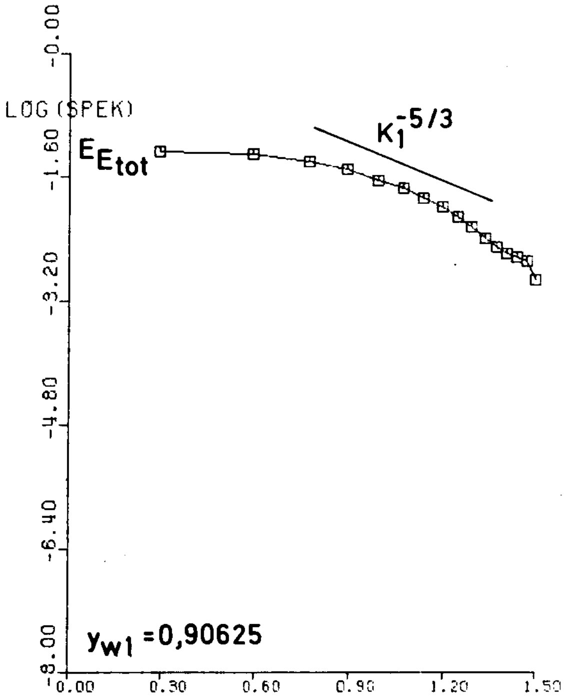

Fig. 52

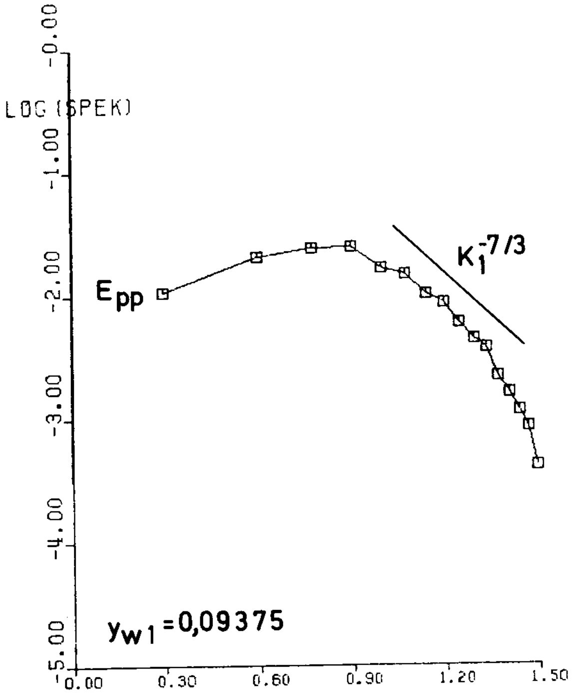

Fig.53

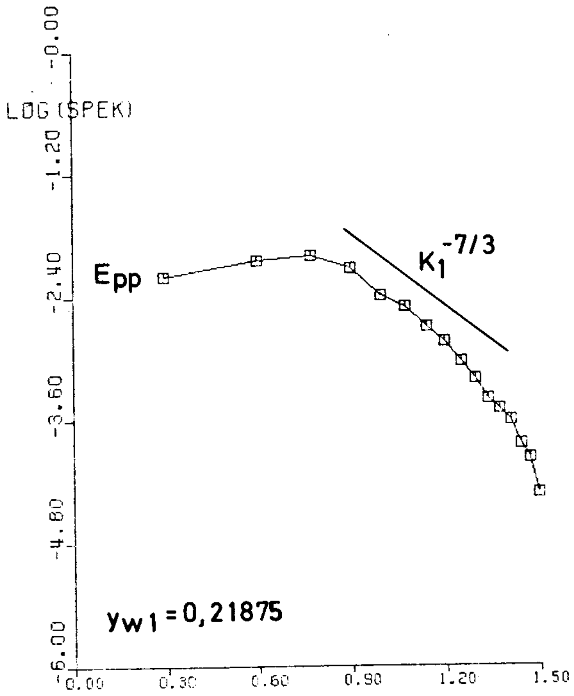

Fig.54

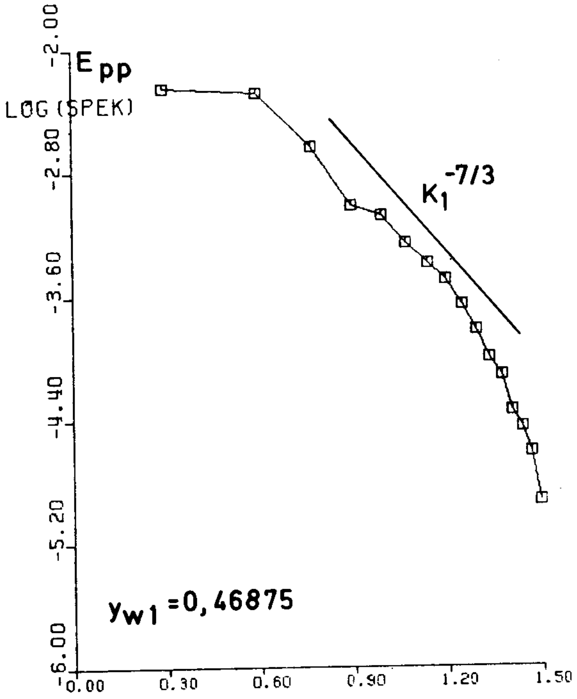

Fig. 55

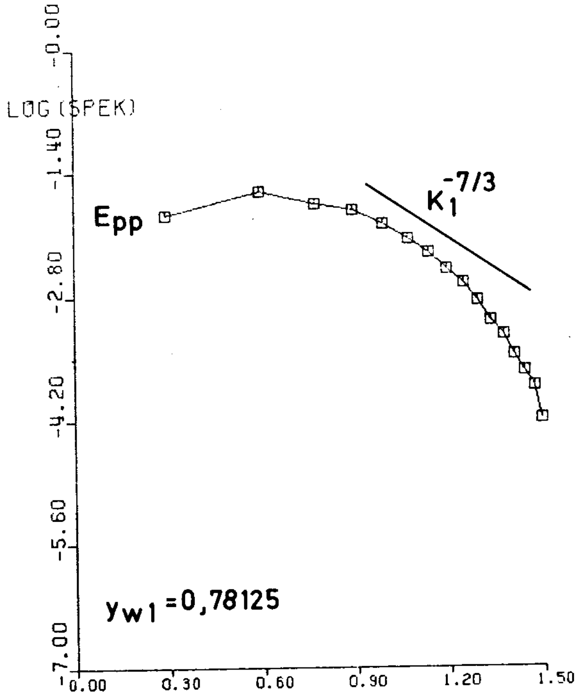

Fig. 56

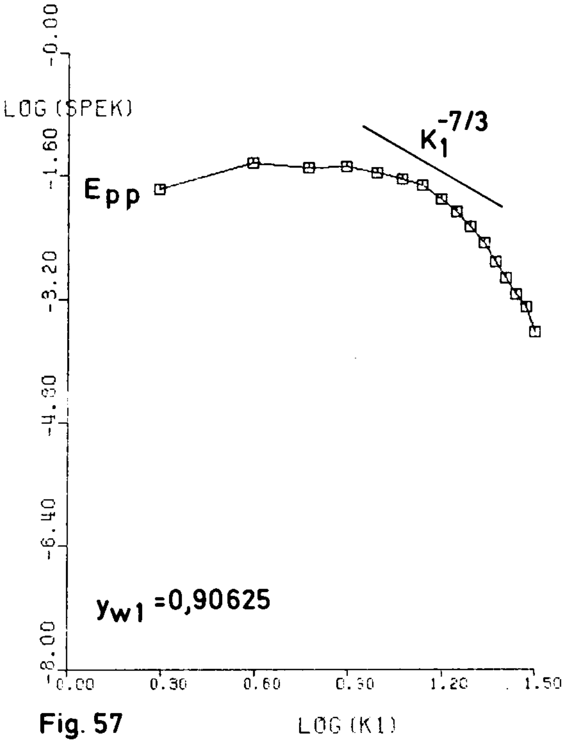

Fig. 57

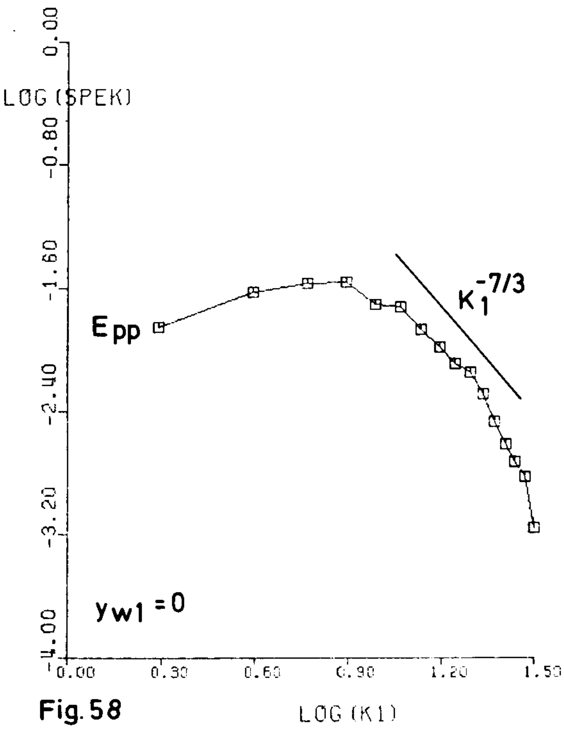

Fig. 58

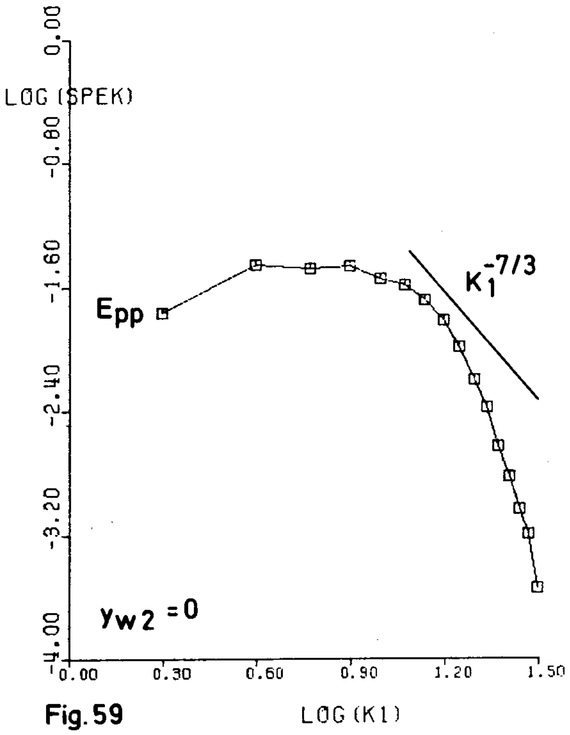

Fig. 59

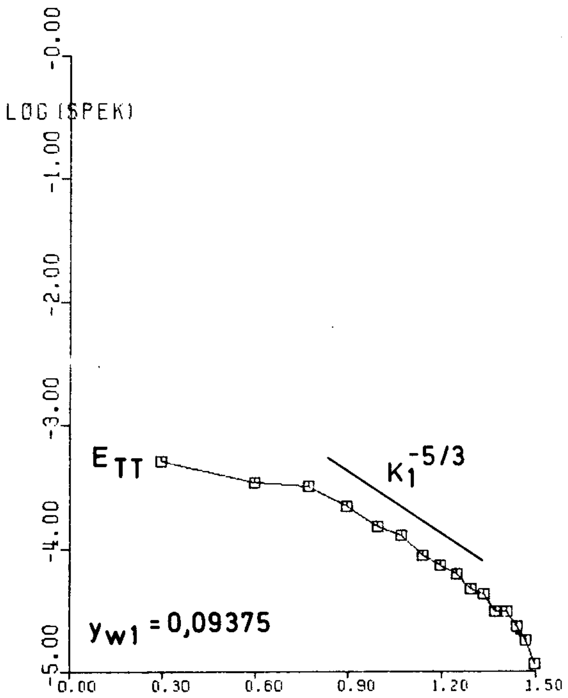

Fig. 60 LOG (K1)

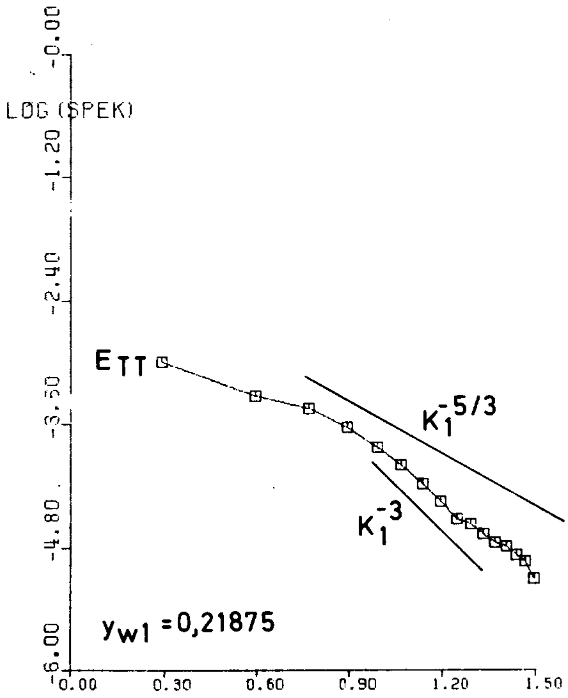

Fig. 61 LOG (K1)

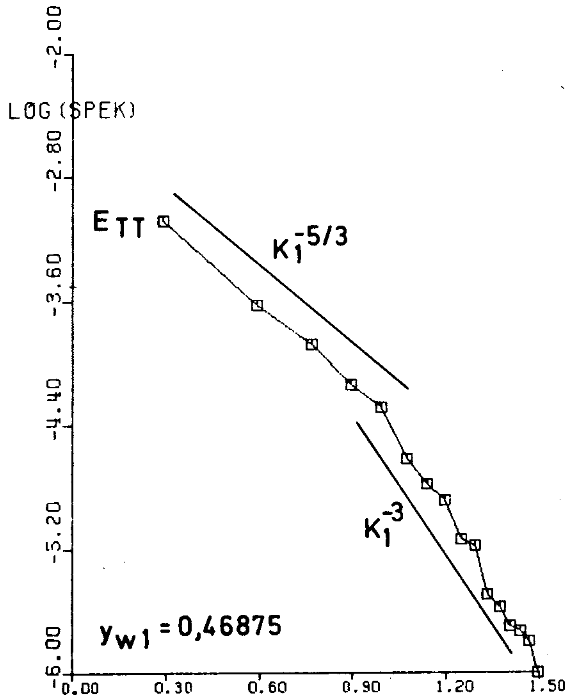

Fig. 62 LOG (K1)

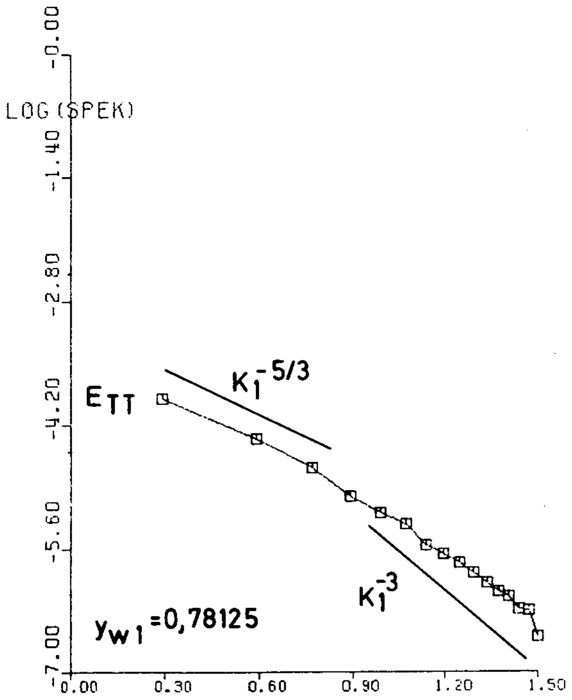

Fig. 63 LOG (K1)

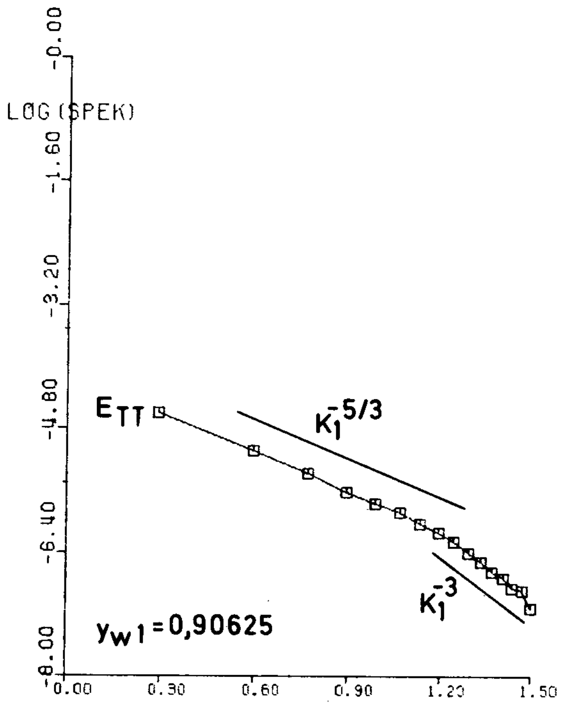
-0.00
LOG (SPEK)
-1.60
-3.20
-4.80
-6.40
-8.00
E_{TT}
$K_1^{-5/3}$
K_1^{-3}
$y_{w1} = 0,90625$
0.00
0.30
0.60
0.90
1.20
1.50
LOG (K1)

Fig. 64